

RESEARCH ARTICLE

Open Access



Subinertial frequency variations in the axis of the Tsugaru Warm Current east of the Tsugaru Strait

Hitoshi Kaneko^{1*} , Takahiro Tanaka², Hiroto Abe^{1,3}, Masahide Wakita¹, Ken'ichi Sasaki¹, Yasumasa Miyazawa⁴, Takeshi Okunishi², Shuichi Watanabe¹, Shoko Tatamisashi¹ and Yoshiaki Sato¹

Abstract

The eastern part of the Tsugaru Strait (located at $\sim 41.5^\circ$ N) is a remarkable region of the coastal flow system around Japan due to the Tsugaru Warm Current (TgWC), an intensive eastward current that flows over its complex topography and exhibits marked tidal variation. The TgWC has a jetlike structure and demonstrates drastic seasonal changes in its path and vertical current structure. Using a high-resolution dataset obtained from a high-frequency radar system (HFR) and a coastal data assimilation experiment (JCOPE-T DA), we focused on the frontal variation, which is shorter than the seasonal timescale, along the axis of the TgWC in relation to the meanders of the jet. We found variations in the axis with multiple timescales between 1 and 14 days, especially in summer and autumn. The ~ 14 -day variation, a remarkable occurrence on the west side of the eastern Tsugaru Strait, was consistent with the tidal variation in the strait. The zonal scale of the axis meander estimated by the HFR matched a scale several times larger than the internal deformation radius, especially in summer and autumn. JCOPE-T DA outputs showed that the crest of such a meander at greater depths progresses in relation to that at the surface. The outputs also suggested instabilities, indicating potential and kinetic energy conversion from the mean to the eddy field. The propagation speed of the several-day variation in the axis estimated from the HFR data was consistent with that of the two-layer baroclinic instability. The several-day variation also showed relatively high coherence with wind variation from summer to autumn, during which time the seasonal wind over the strait switched from easterly to westerly. These variations with multiple timescales imply an effect on north–south water mass mixing in the eastern part of the strait, including rapid acidification in the strait and intensification of stratification.

Keywords: Tsugaru Strait, Tsugaru Warm Current, High-frequency radar, Data assimilation, JCOPE, Frontal waves, Tide, Downfront wind, Baroclinic instability

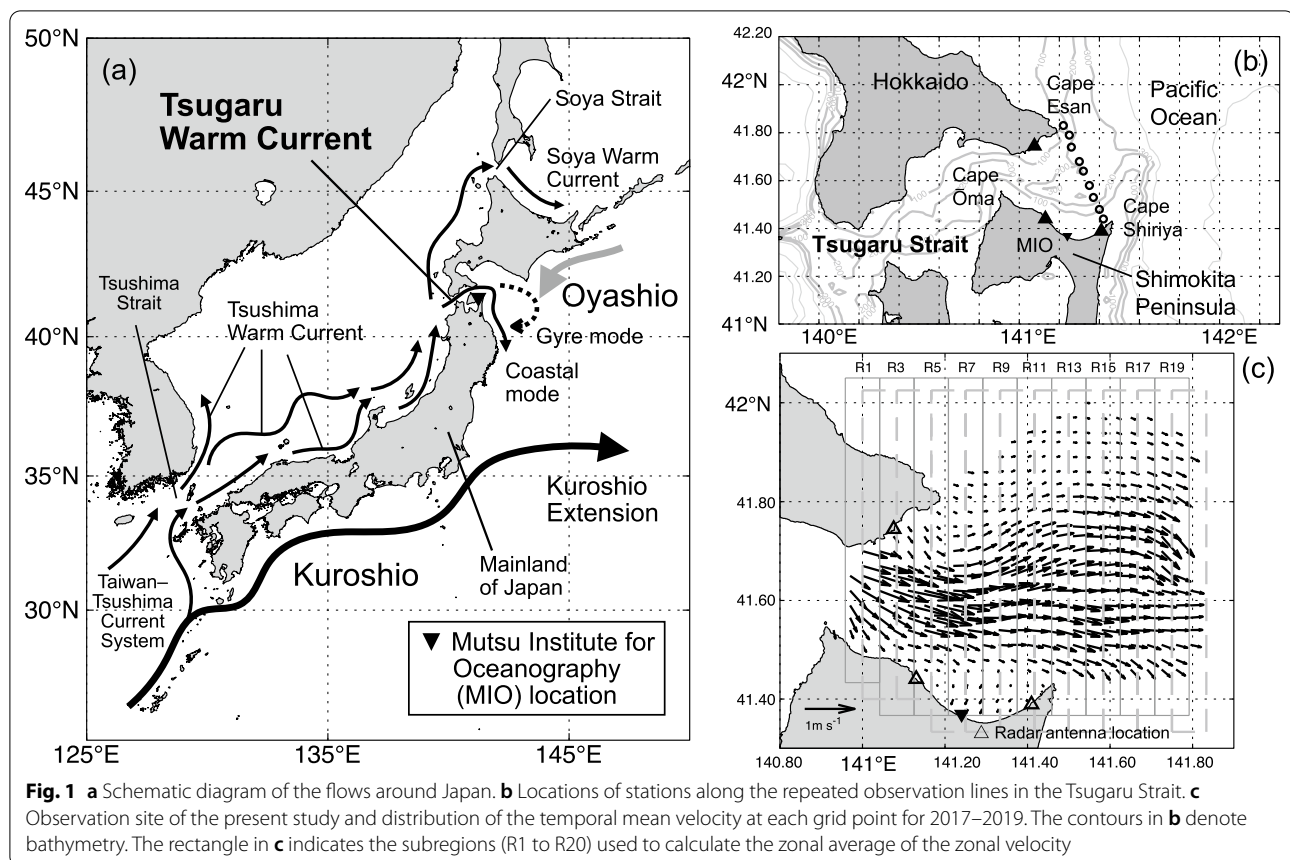
1 Introduction

Ocean currents do not simply flow in a straight path; they are known to meander from time to time. These meanders are caused by a variety of factors, including winds, tides, and complex topography. The Tsugaru Warm

Current (TgWC) flows eastward in the Tsugaru Strait between the mainland of Japan and Hokkaido; it demonstrates remarkable tidal variation over the characteristic topography of the strait (Fig. 1). The volume transport of the TgWC is ~ 1.5 Sv ($= 10^6$ m³ s⁻¹; e.g., Ito et al. 2003; Onishi and Ohtani 1997), and the maximum speed of the eastward velocity reaches 1 m s⁻¹ near the surface in the eastern part of the strait during summer, showing a jet-like structure with intense vertical shear (e.g., Kaneko et al. 2021, hereafter K21).

*Correspondence: h_kaneko@jamstec.go.jp

¹ Mutsu Institute for Oceanography, Research Institute for Global Change, Japan Agency for Marine–Earth Science and Technology (JAMSTEC), 690 Kitasekine, Sekine, Mutsu, Aomori 035-0022, Japan
Full list of author information is available at the end of the article



The TgWC has remarkable seasonal flow pattern variation; due to its horizontal and vertical structure, its path detaches from the coast at times. Recent studies based on high-frequency radar (HFR) observations have indicated that the axis of the TgWC in the eastern part of the strait shifts southward and follows the coast in winter and spring but shifts northward in summer and autumn (Abe et al. 2020; K21; Yasui et al. 2022). This seasonal pattern change is consistent with the development of a large anticyclonic circulation outside the strait in the coastal offshore area of the Pacific, a circumstance referred to as the gyre mode (e.g., Conlon 1982; Rosa et al. 2007; Fig. 1a). Following the theory proposed by Kubokawa (1991), K21 pointed out the impact of the potential vorticity distribution in the upper layer associated with the jet on the seasonal development of the gyre.

In addition to this seasonal variation, shorter-term variations can cause the TgWC to meander in the eastern part of the strait. Tanno et al. (2005) reported that the surface current varies over an ~14-day period in addition to the diurnal tide near Cape Esan (Fig. 1b); this may be the effect of the Mf tide and/or spring–neap tide for the K_1 and O_1 constituents or the “pseudo-Mf tide” due to the nonlinear interaction of dominant diurnal constituents

K_1 and O_1 (Matsuura and Isoda 2020). In addition to such a tidal forcing, wind changes over several days can also generate subinertial frequency variations in the TgWC axis. K21 referred to the possibility that the strengthening of the downfront wind (i.e., westerly wind along the eastward TgWC) dominating in autumn could also generate frontal variations and subsequent instabilities, as suggested by previous studies (mixed layer instabilities; e.g., Boccaletti et al. 2007; Yoshikawa et al. 2012; Thomas et al. 2013).

The meandering current and propagation of such meanders downstream along the current have been reported in other regions, such as the Kuroshio (Kimura and Sugimoto 1993; Itoh and Sugimoto 2008), the Kuroshio Extension (Kouketsu et al. 2005, 2007), and the Gulf Stream (e.g., Brooks and Bane 1981; Lee and Atkinson 1983). Such waves frequently increase in amplitude; eventually, a tongue-like meander detaches from the main stream of the current, entraining warm–lighter (cold–denser) water in the area south (north) of the front as an anticyclonic (cyclonic) eddy (e.g., Yanagi et al. 1998). The origin of the TgWC is thought to be the Kuroshio, which combines with the flow from the Taiwan Strait in the East China Sea (Isobe 1999). The TgWC and its origins

are closely connected through the bifurcated Tsushima Warm Current (TsWC; Kawabe 1982a, b; Wagawa et al. 2020; Yabe et al. 2021) (Fig. 1a). In the eastern part of the strait, a water mass front in the north–south direction has been detected between the warm/saline water of the TgWC and the cold/fresh Coastal Oyashio Water (e.g., Kono et al. 2004; Matsuura et al. 2007; Saitoh et al. 2008; Kuroda et al. 2012; K21). Therefore, if similar waves occur in the strait, such perturbation and subsequent disturbance may influence water exchanges across the front, while also developing stratification. However, observations with sufficient resolution for such frontal waves in the strait are rare—although many repeat observations from ships and moorings are made there—because of the rapid flow velocity of the TgWC and frequent ship traffic through the strait.

Therefore, in the present study, we employ an HFR, which is an effective instrument for the investigation of frontal disturbances, including eddies (e.g., Schaeffer et al. 2017), as in K21. In addition, we use model output from a high-resolution assimilation system (2–3 km) that assimilates various satellite and in situ observed data without the above-mentioned HFR data (a downscaled and assimilated version of the Japan Coastal Ocean Predictability Experiment, tide enabled; JCOPE-T DA; Miyazawa et al. 2021). Data obtained from these systems allow us to determine the impacts of frontal disturbances on shorter-than-seasonal timescales.

The remainder of this paper is organized as follows. In the next section, we provide details of the data, including the HFR, numerical model, and shipboard observations. Estimation methods in relation to instabilities are also described, including the potential vorticity, energy conversion rate, and propagation speed of the baroclinic instability, based on the theories provided by previous studies (e.g., Pedlosky 1987; Vallis 2006). In Sect. 3, we first demonstrate the seasonal variation in the strait by comparing the results obtained from the observations and the numerical model. Then, we investigate the variations in the subinertial frequency and horizontal characteristics of the meanders. Subsequently, the possibility of instabilities is examined based on JCOPE-T DA outputs. These results are discussed further in Sect. 4 using observational data, and our conclusions are provided in Sect. 5.

2 Methods

2.1 Velocity from high-frequency radar

To monitor the surface current in the eastern part of the Tsugaru Strait, the Mutsu Institute for Oceanography (MIO), Japan Agency for Marine–Earth Science and Technology (JAMSTEC), installed a monitoring system using an HFR (CODAR, SeaSonde, 13.9 MHz; Fig. 1b

and c; K21). The HFR provides data with a horizontal resolution of ~ 3 km over an area from ~ 3 to 60 km from each antenna (Fig. 1c). The surface current distribution is calculated approximately every 30 min by the system and uploaded to the MIO Ocean Radar data Site for the Eastern Tsugaru Strait (MORSETS; <http://www.godac.jamstec.go.jp/morsets/e/top/>). In the present study, we employed data from 2017 to 2019 when all three antennas were operating normally (monitoring started in 2014).

K21 reported that the accuracy of the zonal velocity of the HFR was $20 \times 10^{-2} \text{ m s}^{-1}$ along the Shiriya–Esan line (SE line) via comparison with the acoustic Doppler current profiler mounted on some ships (SADCP) velocity obtained from repeated shipboard observations along the SE line (Fig. 1b). The same type of HFR (CODAR, SeaSonde, 13.9 MHz) has been used for surface current monitoring at the Tsushima Strait (Yoshikawa et al. 2006, 2010) and at the Soya Strait (Ebuchi et al. 2009; Fig. 1a). Yoshikawa et al. (2006) mentioned that the root-mean-square velocity difference between the HFR and SADCPs calculated from principal component analysis was $6.62\text{--}11.3 \times 10^{-2} \text{ m s}^{-1}$ in the Tsushima Strait. Ebuchi et al. (2009) reported that the current estimated from the HFR agreed well with those derived from SADCPs with root-mean-square differences less than $25 \times 10^{-2} \text{ m s}^{-1}$ in the Soya Strait. We excluded grids with data acquisition rates of $< 75\%$ over the duration of the analysis.

2.2 Data assimilation model

To compare the results obtained from the HFR, we also used outputs calculated by the JCOPE-T DA data assimilation system (Miyazawa et al. 2021). The JCOPE-T DA system provides hourly output of variables, including sea level, temperature, salinity, and ocean current velocities, at a horizontal resolution of $1/36^\circ$ and 46 active sigma coordinate levels in the vertical direction (Miyazawa et al. 2021). We converted the vertical level of the data (temperature, salinity, and velocities) to z-coordinates at 5-m intervals, focusing on the $41.0^\circ \text{ N}\text{--}42.5^\circ \text{ N}$, $140.5^\circ \text{ E}\text{--}142.5^\circ \text{ E}$ region from June 5, 2018, to December 31, 2019. The model included volume fluxes and sea level anomalies for 11 tidal constituents (Q1, O1, P1, K1, N2, M2, S2, K2, M4, MS4, and MN4) at the lateral boundaries. Moreover, the surface pressure gradient included the equilibrium gradient due to 25 potential tidal constituents (Q1, O1, M1, P1, K1, J1, OO1, 2N2, MU2, N2, NU2, M2, L2, T2, S2, K2, M4, MS4, MN4, MM, MF, SSA, SA, MTM, and MSQM). The atmospheric forcing data were obtained from the National Centers for Environmental Prediction global forecast system. More details about the

JCOPE-T DA configuration may be found in Miyazawa et al. (2021).

2.3 Shipboard observations and other data

To validate the subsurface fields in the strait with those estimated from the JCOPE-T DA, we employed the seasonal mean estimated repeated shipboard observations along the SE line. Observations were conducted along the SE line (Fig. 1b, Table 1) in almost every season from 2009 to 2019 by three ships: the training ship (T/S) *Ushio-Maru* and T/S *Oshoro-Maru* belonging to Hokkaido University and the research vessel (R/V) *Wakataka-Maru* belonging to the Japan Fisheries Research and Education Agency (Table 2). Observations of temperature, salinity, and pressure were obtained as conductivity–temperature–depth (CTD) observations during the cruises using an SBE 911 plus (Sea-Bird Scientific, Inc.).

Moreover, to estimate variations in some tidal components, such as M_2 , K_1 , and O_1 , through harmonic

analysis, we employed the hourly sea level data distributed by the Japan Meteorological Agency at MIO for 2017–2019 (41.37° N, 141.23° E; <https://www.data.jma.go.jp/kaiyou/db/tide/genbo/index.php>). For comparison with the results from the JCOPE-T DA, we also employed local wind data at Cape Shiriya, Esan, and Ōma (Fig. 1b) obtained from the Japan Oceanographic Data Center online archive (<https://jdoss1.jodc.go.jp/vpage/wave.html>) for 2017–2019. We used bathymetry estimated from ETOPO1 (National Oceanic and Atmospheric Administration (NOAA) National Geophysical Data Center. 2009: ETOPO1 1 Arc-Minute Global Relief Model. NOAA National Centers for Environmental Information. Accessed on 23 June 2021; Amante and Eakins 2009).

2.4 Analysis methods

First, for analysis of the HFR data, we defined 20 subregions aligned in the north–south direction (Fig. 1c; R1–R20) and calculated the spatial means of zonal velocity at each latitude in the east–west direction in each subregion. We also calculated the 24-h running mean of this time series at each latitude in each subregion. Then, the latitude of the maximum mean zonal velocity along the north–south direction was defined as the axis of the TgWC (the same detection method was adapted for the JCOPE-T DA zonal velocity). The temporal mean and standard deviation of the axis latitude in each season were estimated from the HFR. In this study, winter was defined as January–March, spring as April–June, summer as July–September, and autumn as October–December.

Table 1 Locations of the stations with repeated shipboard observations

Station	Latitude (°N)	Longitude (°E)
SE1	41.44	141.42
SE2	41.48	141.40
SE3	41.53	141.37
SE4	41.58	141.35
SE5	41.64	141.32
SE6	41.68	141.30
SE7	41.74	141.26
SE8	41.79	141.25
SE9	41.83	141.22

Table 2 Implementation record of hydrographic observations along the Shiriya–Esan (SE) line. U, O, and W represent the observations made by T/S *Ushio-Maru*, T/S *Oshoro-Maru*, and R/V *Wakataka-Maru*, respectively

Year	Winter			Spring			Summer			Autumn		
	Jan	Feb	Mar	Apr	May	Jun	Jul	Aug	Sep	Oct	Nov	Dec
2009											U	
2010		U			U			U			U	
2011		O			U		U				U	
2012		U				U		U			U	
2013					U			U				
2014		U			U			U			U	
2015		U	U		U						U	
2016		U			U	U					U	
2017					U							
2018		U						W				
2019				U					W		U	

The potential density and its anomaly, σ_θ , were calculated using the temperature, salinity, and pressure values following Gill (1982). Then, the buoyancy frequency (N) was defined as follows:

$$N^2 = -\frac{g}{\rho} \frac{\partial \sigma_\theta}{\partial z}, \quad (1)$$

where g and ρ are the gravitational acceleration (9.8 m s^{-2}) and potential density, respectively. Then, the seasonal mean geostrophic velocity between adjacent stations was calculated using the isodepth mean obtained from the shipboard observations for each season, following Pond and Pickard (1986).

We calculated the power spectrum of the axis variation, $P(f)$, after a 24-h running mean at each subregion (R1–R20) for each season (90 days). Then, we calculated the ratio of $P(f)$ for each subperiod to sum $P(f)$, that is, R_p , and $R_{P(f_1, f_2)}$ as follows:

$$R_{P(f_1, f_2)} = \frac{\sum_{yr_1}^{yr_2} \sum_{f_1}^{f_2} P(f) \Delta f}{\sum_{yr_1}^{yr_2} \sum_{f_f}^{f_e} P(f) \Delta f}, \quad (2)$$

where yr_1 and yr_2 are 2017 and 2019, respectively. Here, f_f and f_e are the 1/90 cycle per day (cpd) and 1 cpd, respectively. We calculated $R_{P(f_1, f_2)}$ for the three cases: $f_1 = 1/15$ cpd and $f_2 = 1/12$ cpd; $f_1 = 1/10$ cpd and $f_2 = 1/5$ cps; and $f_1 = 1/5$ cpd and $f_2 = 1/1$ cpd.

To examine the perturbations that vary with timescales of several days, likely due to wind over the strait, we applied a bandpass fourth-order Butterworth filter to the axis variation with cutoff timescales of 1.3 days and 3 days (see subsection 4.1 for this period selection). Then, we analyzed the lagged correlations of the time series data for some seasons (summer and autumn) using the bandpass-filtered data. The lagged correlations were calculated for each subregion with respect to the reference subregion (Fig. 1c). The timescale of the correlation peaks was regarded as the lag of perturbation arrival, and by using the distance between the reference subregion and each subregion, the propagation speed of the perturbation was estimated in summer and autumn of each year during 2017–2019.

To investigate whether the necessary conditions of instabilities (Charney and Stern 1962; Pedlosky 1964) could actually be satisfied, we calculated potential vorticity based on the JCOPE-T DA outputs as follows. First, we estimated stream function, ψ , as an integral of temporal mean zonal velocity, U , from the south bank of the strait to the north direction. Then, we calculated the potential vorticity, Q , as follows:

$$Q = -\frac{\partial U}{\partial y} + \frac{\partial}{\partial z} \frac{f_{41.5^\circ N}^2}{N^2} \frac{\partial \psi}{\partial z}. \quad (3)$$

Here, we assumed that β is 0 since the meridional width of the eastern part of the Tsugaru Strait is narrow ($\sim 0.4^\circ$ latitude around the SE line, although the north boundary is open east to 141.2° E ; Fig. 1b), and we assumed that the zonal velocity component of relative vorticity dominates the meridional component. Furthermore, $f_{41.5^\circ N}$ is the inertial frequency at 41.5° N . Then, we compared the distribution of the differential of Q in the meridional direction, Q_y , with that of the vertical shear of the zonal velocity, U_z . We tested one case as an example during July 26–27, 2019, when a marked meandering was shown.

Using the data obtained from the JCOPE-T DA, we also estimated the energy conversion rates between the eddy and mean fields for each season as follows (e.g., Brooks and Niiler 1977; Dewar and Baine 1989; Kang and Curchitser 2015):

$$\text{MKE to EKE} : C'_k = -\overline{u'u'} \frac{\partial \bar{u}}{\partial x} - \overline{u'v'} \left(\frac{\partial \bar{u}}{\partial y} + \frac{\partial \bar{v}}{\partial x} \right) - \overline{v'v'} \frac{\partial \bar{v}}{\partial y}, \quad (4)$$

$$\text{MPE to EPE} : C'_p = -\frac{g}{\rho_0} \overline{u'\rho'} \frac{\partial \bar{\rho}}{\partial x} \frac{\partial \bar{\rho}}{\partial z} \Big|^{-1} - \frac{g}{\rho_0} \overline{v'\rho'} \frac{\partial \bar{\rho}}{\partial y} \frac{\partial \bar{\rho}}{\partial z} \Big|^{-1}. \quad (5)$$

Here, u and v denote zonal and meridional velocities (24-h-running-mean filtered), respectively, and overbars and primes indicate the temporal mean and anomalies from the temporal mean, respectively. MKE, EKE, MPE, and EPE denote the mean kinetic energy, eddy kinetic energy, mean potential energy, and eddy potential energy, respectively. Positive values denote energy transfer from the mean field to the eddy field in Eqs. 4 and 5. Each component of Eq. 4 is interpolated to the longitude/latitude of the temperature and salinity grid for the JCOPE-T DA.

Next, we estimated the theoretical propagation speed of the baroclinic instability for comparison with that of the meanders detected by the HFR observation assuming a flat bottom. Following K21, we calculated vertical normal modes (e.g., Gill 1982; Emery and Thomson 2001) and defined the upper layer depth H_1 as the node depth of the first vertical mode. Then, following the derivation of Pedlosky (1987; his Eq. 7.11.9), the phase speed of the baroclinic instability in the case of zero planetary beta ($\beta=0$) in the two-layer stratified model may be written as follows:

$$c = \frac{U_1(K^2 + 2/R_2^2) + U_2(K^2 + 2/R_1^2)}{2(K^2 + 1/R_1^2 + 1/R_2^2)} \pm \frac{(U_1 - U_2)(4/R_1^2 R_2^2 - K^4)^{1/2}}{2(K^2 + 1/R_1^2 + 1/R_2^2)} i, \quad (6)$$

where K , U_1 , U_2 , and i are the total wavenumber, the mean velocity of the upper and lower layers, and the imaginary unit, respectively. Here,

$$\frac{1}{R_n^2} = \frac{f_{41.5^\circ N}^2}{g' H_n}, \quad (7)$$

where H_n is the thickness of the n th layer (we assumed a mean water depth of 250 m, and H_2 was estimated as 250 minus H_1) and g' is the reduced gravity calculated from the eigenvalue of the first vertical normal mode c_{1st} and H_1 as c_{1st}^2/H_1 (K21). Instability occurs when $K^2 < 2/R_1 R_2$ (that is, $4/R_1^2 R_2^2 > K^4$). Assuming that the wavenumber of the perturbation observed in the strait is sufficiently small for such instability, we employed the propagation speed of the instability (real part of Eq. 6), as mentioned in Itoh and Sugimoto (2008), as follows:

$$c = \frac{U_1(K^2 + 2/R_2^2) + U_2(K^2 + 2/R_1^2)}{2(K^2 + 1/R_1^2 + 1/R_2^2)}. \quad (8)$$

This equation indicates that the propagation speed, c , is a value between U_1 and U_2 . If we assume that the horizontal wavenumber K is far smaller than $1/R_n^2$, $1/R_n^2$ would be regarded mathematically as the weighting function. Notably, however, the wavelength at which it grows the most is several times as long as the internal deformation radius, as described below. In the present study, U_1 and U_2 were estimated in two ways: from the shipboard observations and from the JCOPE-T DA output. From the shipboard observations, the spatial mean of the geostrophic velocity in the upper and lower layers along the SE line was employed. It should be noted that we changed the zonal range of the mean for U_1 and U_2 for each season, considering the seasonal structure of the TgWC. That is, we extracted the strong eastward current part of the TgWC. For the geostrophic velocity case, we used the range SE4–SE8 in summer and SE3–SE6 in autumn. From the model output, the meridional average from 41.575°N (41.55°N) to 41.75°N (41.7°N) in each layer at 141.3°E was used in summer (autumn).

For wavenumber K , we first assumed that the perturbation has a length scale similar to that of the fastest growing baroclinic instability in the two-layer model: $\lambda = 2\pi L_D/1.79$ (e.g., Vallis 2006). Here, L_D is the internal deformation radius calculated from the eigenvalue of the first mode of the vertical normal mode, which is equivalent to the phase speed of the internal gravity wave (first baroclinic mode) and the Coriolis parameter at 41.5°N ($L_D = c_{1st}/f_{41.5^\circ N}$; K21). Then, we defined $K = 2\pi/\lambda$. We also considered the wavelength of Eady's case, $\lambda' = 2\pi L_D/1.61$ (Eady 1949; Gill 1982), for comparison with the zonal scale of meanders of the TgWC axis estimated from the HFR and JCOPE-T DA data. The zonal scale of meanders

of the TgWC axis L_p was defined as the adjacent peak distances (i.e., “crests”) of the axis latitude. Comparing the difference between the first peaks at the surface from 141.0°E and the lower depths, such as 50 m and 150 m (D_p) to L_p , we estimated a vertical shift of the wave crest using the JCOPE-T DA data.

3 Results

3.1 Seasonal change in the internal structure in the eastern part of the strait

The seasonal mean distributions of the temperature, salinity, and σ_θ obtained from shipboard observations show characteristic seasonal changes, as reported by a previous study (e.g., Nishida et al. 2003; K21; Yasui et al. 2022; Fig. 2a–d). That is, (1) higher (lower) temperature and salinity water is generally observed on the southern (northern) side, which corresponds to the water transported by the TgWC (the water modified by the Oyashio Water and/or Coastal Oyashio Water) [according to Hanawa and Mitsudera 1987, the TgWC Water, Oyashio Water, and the Coastal Oyashio Water are defined as T (temperature) $> 5^\circ\text{C}$ and $33.7 < S$ (salinity) < 34.2 , $T < 7^\circ\text{C}$ and $33.0 < S < 33.7$, and $T < 2^\circ\text{C}$ and $S < 33.0$, respectively]; (2) the vertical gradient of the temperature is larger in summer and smaller in winter (when the stratification is weak in winter, H_1 generally becomes larger beneath all stations); and (3) the isotherms are generally parallel to those of σ_θ and cross with isodepths of approximately 41.5–41.7° N, especially in summer and autumn. The characteristics of the north–south water mass distribution and the seasonal changes in the stratification are well represented by the JCOPE-T DA section along 141.3°E (Fig. 2e–h).

As reported in K21, the seasonal change in the zonal velocity structure, based on a SADC (not shown here), is also represented well by geostrophic velocity along the SE line (Fig. 3a–d) except for winter: eastward flow occurs near the southern boundary during spring and a northward shift of the TgWC axis occurs in summer and autumn. These features are also reproduced by the JCOPE-T DA along the 141.3°E section (Fig. 3e–h). Furthermore, during the summer and autumn seasons, in addition to marked eastward flow ($> 1.0 \text{ m s}^{-1}$) near the center of the strait, westward flow ($< -0.2 \text{ m s}^{-1}$) between the axis and the Shimokita Peninsula is also represented (Fig. 3c d, and g). Eddy kinetic energy (EKE), defined as the squared sum of anomaly velocities from the seasonal temporal mean, $\text{EKE} = 1/2 (u'^2 + v'^2)$, shows greater values during summer and autumn than during winter and spring, especially near the surface (Fig. 3e–h). The vertical difference in the seasonal mean of the zonal velocity between the upper and lower layers (surface to H_1 and H_1 to bottom, respectively;

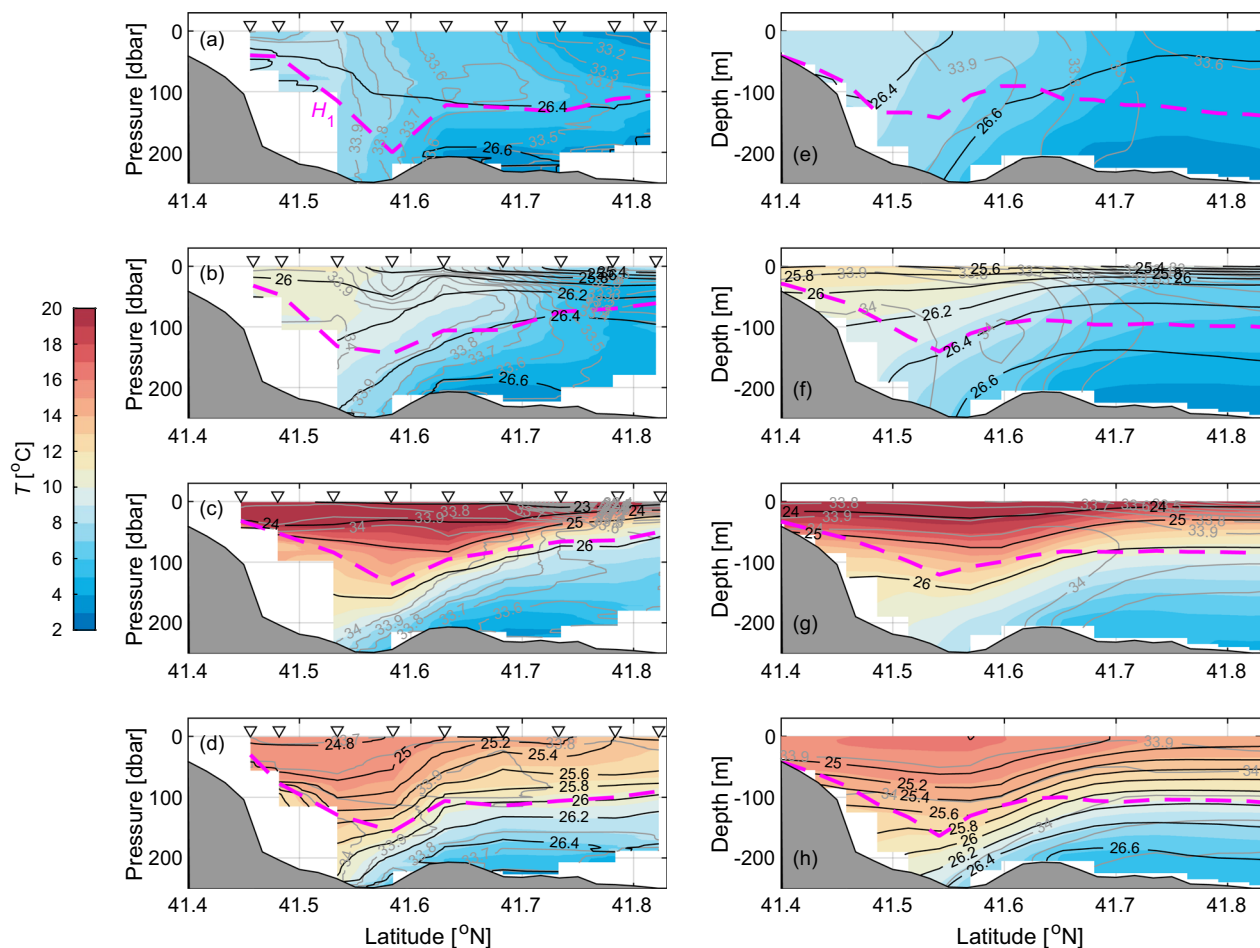


Fig. 2 Vertical transect of seasonal means of temperature (color), salinity (gray contours), and potential density anomaly, σ_θ (black contours), obtained from the shipboard observations along the Shiriya–Esan line (estimated from the JCOPE-T DA data) in **a** (e) winter, **b** (f) spring, **c** (g) summer, and **d** (h) autumn, shown in the left (right) column. Triangles shown in the left column are the latitude of each station. The dashed magenta line is the depth of the upper layer, H_1

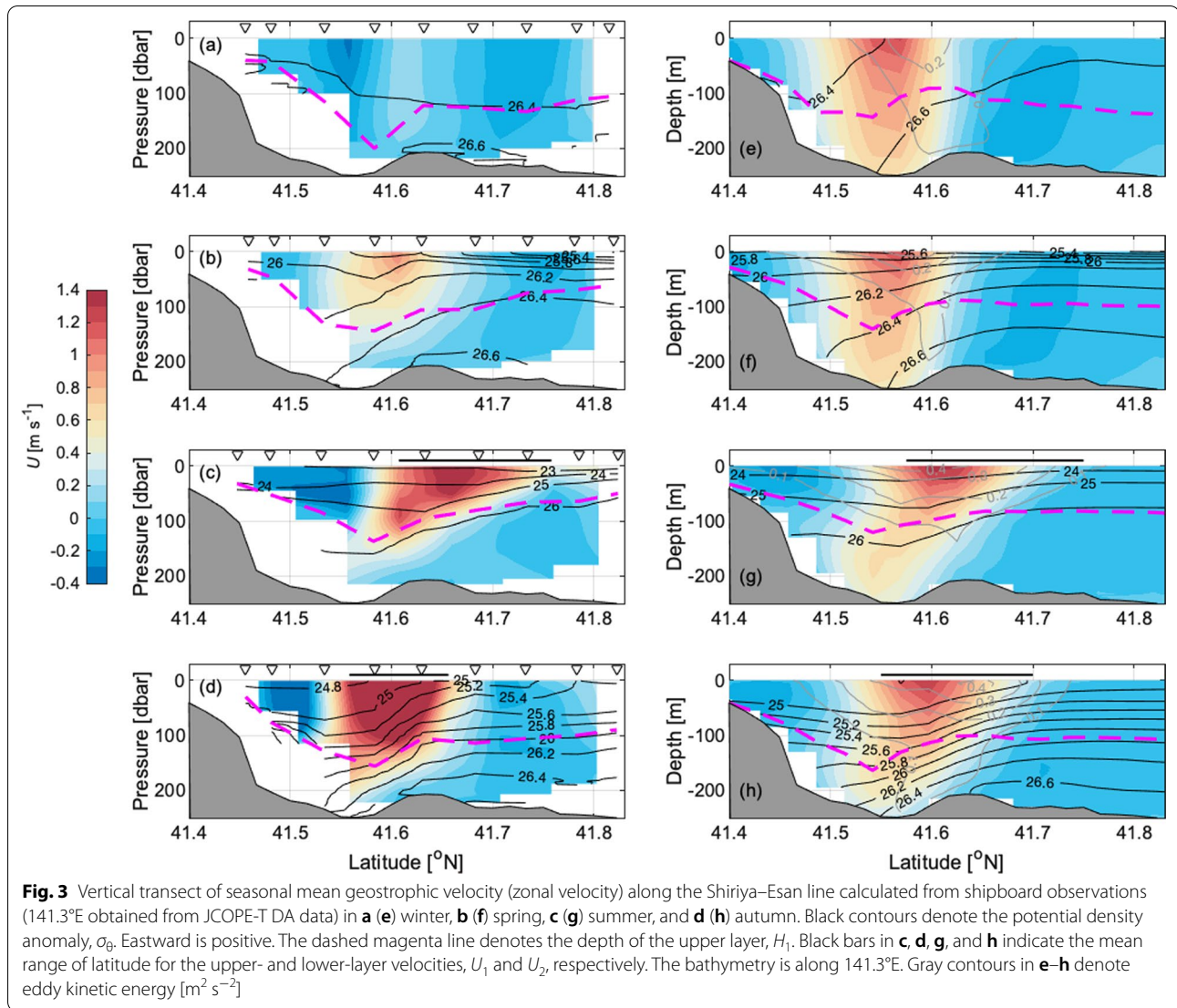
meridional range of mean: 41.5–41.7°N) becomes largest in summer and autumn ($\sim 0.3 \text{ m s}^{-1}$) and smallest in winter ($< 0.1 \text{ m s}^{-1}$) according to the JCOPE-T DA output (Additional file 1: Fig. S1).

3.2 Seasonal and shorter timescale variation in the Tsugaru Warm Current axis

The HFR data indicate seasonal shifts of the axis of the TgWC as reported by previous studies (e.g., Rosa et al. 2007; Abe et al. 2020; K21; Yasui et al. 2022): for 141.1° E–141.5° E, the shift occurs south of 41.6° N in winter and spring (Fig. 4a and b) and north of 41.6° N in summer and autumn (Fig. 4c and d). Then, the contrast in the relative vorticity across the axis becomes remarkable in summer at 141.2–141.4° E (Fig. 4c). The seasonal change in the axis location and increase in the contrast of the relative vorticity are also represented by the

JCOPE-T DA outputs (Fig. 5). The longitude–time distributions estimated from both HFR and the JCOPE-T DA along the nearest transection of 141.3° E also show very similar seasonal changes in the axis latitude, as mentioned above (Fig. 6). Thus, the temporal variation in the axis latitude estimated from the JCOPE-T DA data seems to properly represent its seasonal variation.

Apart from the seasonal movement of the axis mentioned above, shorter-term oscillation within several dozen days is also observed (Fig. 6). We applied a wavelet transform to the latitude of the TgWC axis at 141.3° E longitude (Fig. 7). The wavelet transforms estimated from both the HFR data and the JCOPE-T DA data indicate maxima around a frequency of 0.07 cpd (a period of 14 days) and at 1 cpd (period of 1 day). In addition to this 0.07 cpd variation for the whole season, seasonal enhancement of the amplitude is also evident in the



wavelet transforms between frequencies of 0.07 cpd and 1 cpd (period between 14 days and 1 day) (Fig. 7). The seasonal enhancement from summer to autumn is clearly represented in the wavelet transform of the JCOPE-T DA (Fig. 7b). Although the wavelet transform obtained from the HFR suggests some maxima for 0.2–1 cpd (1 day to 5 days) during winter to early spring (from January to April), it is not clearly evident in the wavelet transform obtained from the JCOPE-T DA.

The variation in the TgWC axis with a 14-day timescale is consistent with that of the current near Cape Esan (Tanno et al. 2005). Thus, we also examined the coherence of the axis variation obtained from the HFR in each subregion (Fig. 1c) for 2017–2019 in relation to that at the reference subgrid, R1 (Fig. 8a). Remarkable coherence (>0.4) is shown at 14 days from 141.0 to 141.6° E,

although the phase difference $|\phi/\pi|$ increased from 141.0° E ($|\phi/\pi| \sim 0$) to 141.6° E ($|\phi/\pi| \sim 1$). For comparison, we also calculated the coherence of the axis variation at each subgrid to that at R8 (nearest 141.3° E) (Fig. 8b). Then, in addition to 14 days, marked coherence is shown at 8 days and approximately 5 days, suggesting subinertial frequency variation generated at approximately 141.3° E.

It is expected that tides affect the axis latitude variation by 14 days (Tanno et al. 2005; Matsuura and Isoda 2020). Thus, we compared the time series of the axis variation at 141.3° E (12- and 15-day bands passed one) to the timing of spring and neap tides, as well as the time series of the Mf tide component estimated from the harmonic analysis of sea level data at MIO (Additional file 1: Fig. S2; another case of the K_1 and O_1 tide components is also shown in Additional file 1: Fig. S3). The results show that the phase

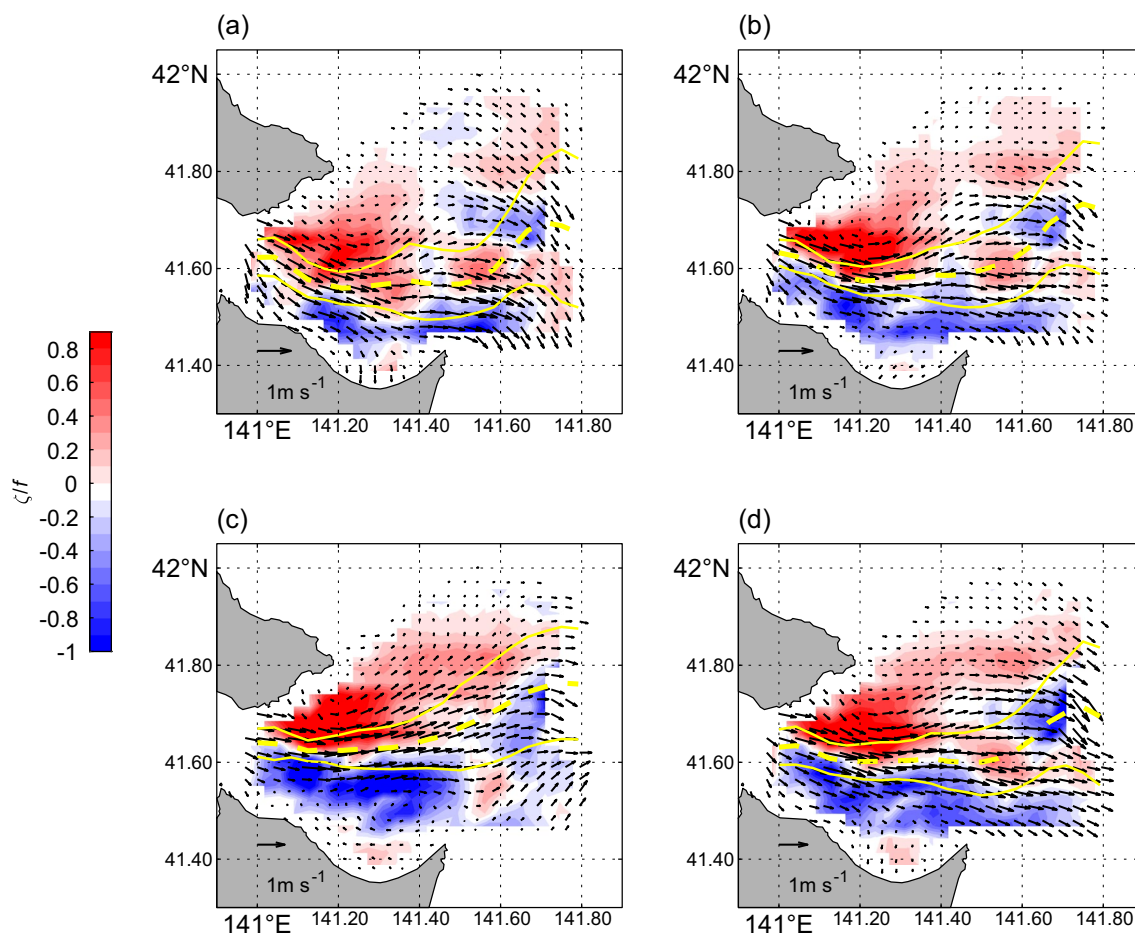


Fig. 4 Seasonal mean of the surface velocity obtained from the high-frequency radar data in **a** winter, **b** spring, **c** summer, and **d** autumn. The color denotes the relative vorticity estimated from the radar data as $\partial v/\partial x - \partial u/\partial y$, where u and v are the zonal and meridional velocities, respectively. The yellow dashed (solid) line shows the temporal mean (standard deviation) of the Tsugaru Warm Current axis. The bathymetry is along 141.3°E

of the axis variation is inversely synchronized with the phase with Mf variation (with variation in the envelope of the K_1 and O_1 variation). Wavelet analysis of the variation in the TgWC axis at each subgrid in relation to the Mf variation shows robust coherence for 141.0 – 141.6°E from April to September of each year (Additional file 1: Fig. S4a). This seasonal variation in coherence is consistent with the result of Tanno et al. (2005) [based on this seasonality, the amplitude difference of the axis amplitude in January among 2017, 2018, and 2019 (Additional file 1: Figs. S2 and S3) may also be explained by the winter density distribution because a weakly stratified condition in relation to the general winter was observed in 2018 (not shown)]. The phase difference of the wavelet cross spectrum shows that the phase difference is smaller at 141.4 – 141.6°E than at 141.0 – 141.2°E (Additional file 1: Fig. S4a; note that the longitude of MIO is 141.24°E). $R_{P(f_1, f_2)}$ for 12–15 days tends to decrease with increasing longitude, especially in summer and autumn

at 141.8°E (Additional file 1: Fig. S4b–e; 10–25% at 141.2°E to <10% at 141.8°E). In contrast, the longitudinal trend of $R_{P(f_1, f_2)}$ for 5–10 days is more ambiguous than that for 12–15 days (Additional file 1: Fig. S4b). $R_{P(f_1, f_2)}$ for 1–5 days is also similar to that for 12–15 days at approximately 141.3°E in summer and autumn (10–20%), suggesting the importance of the subinertial frequency with 1–10-day variation in the axis fluctuation in the region distanced from the topography (i.e., the outlet of the channel at 141.1°E , Fig. 1c).

3.3 Features of axis meandering in the eastern part of the strait

Since the subinertial frequency variation in the TgWC axis and phase change along the downstream direction have been shown in the eastern part of the Tsugaru Strait (Fig. 8), we focused on the zonal scale of such variations considering propagation disturbances. By extracting the first and second peaks of the meanders from 141.0°E to

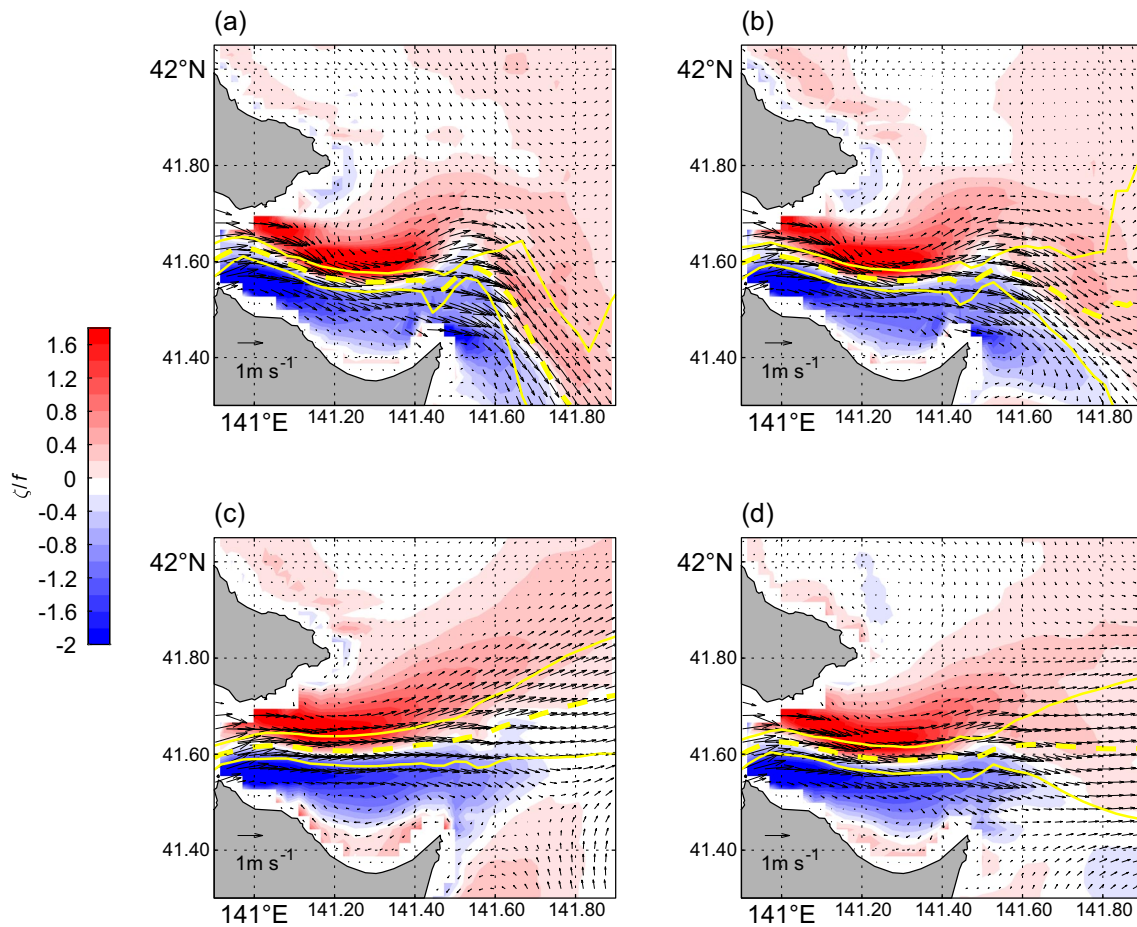


Fig. 5 Seasonal mean of the surface velocity obtained from the JCOPE-T DA data in **a** winter, **b** spring, **c** summer, and **d** autumn. The color and yellow lines are the same as those in Fig. 4

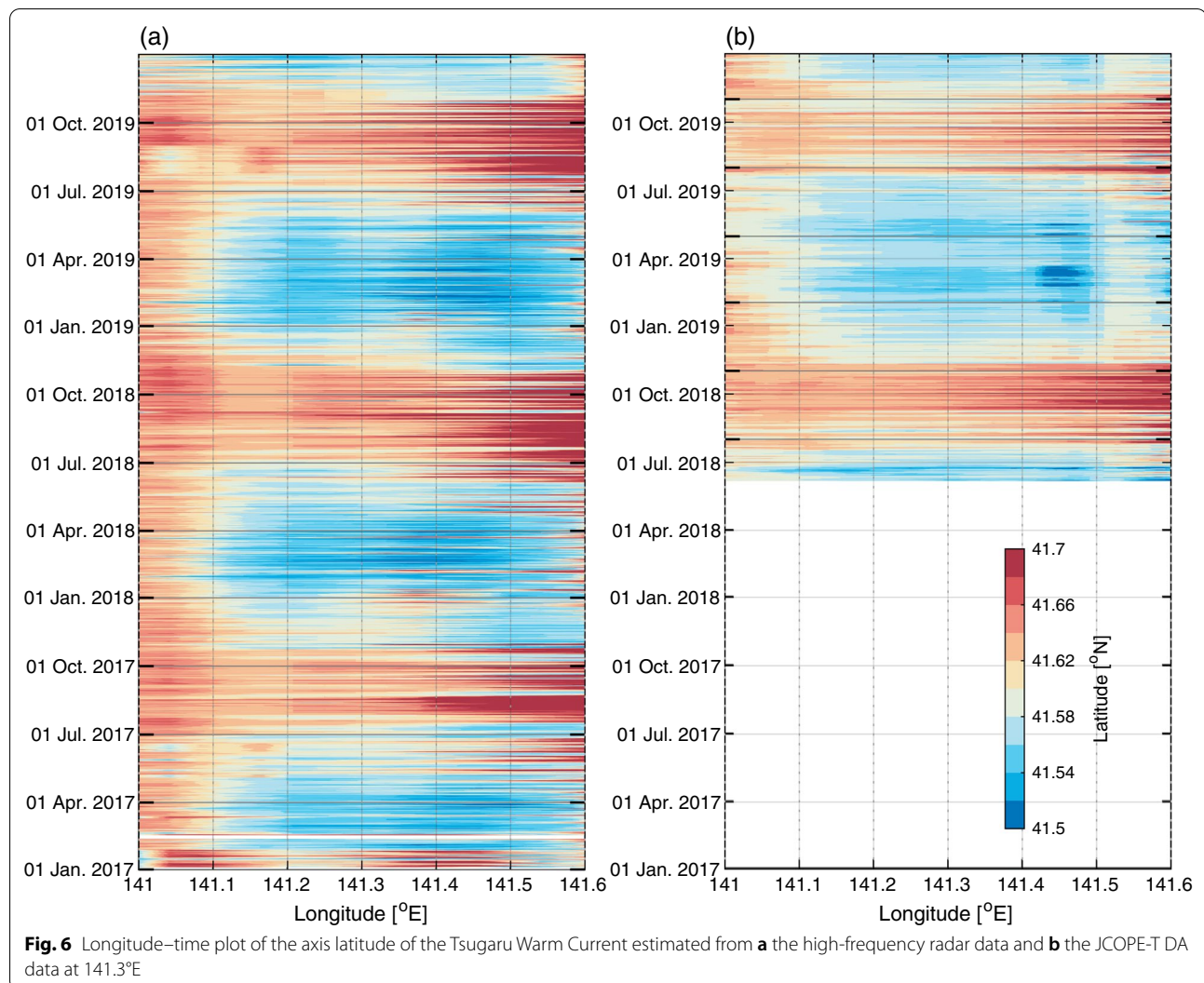
downstream, we examined the frequency distribution of the ratio of the zonal scale of adjacent peaks (L_p) to the internal deformation radius (L_D) in each season (Fig. 9). In the frequency distribution of L_p/L_D (subpanels in Fig. 9), the peak of L_p/L_D seems to be larger than $2\pi/1.79$ (two-layer case) in winter (Fig. 9a) and spring (Fig. 9b). However, the peak of L_p/L_D is located at approximately $2\pi/1.79$ in summer and autumn (Fig. 9c and d, respectively). This result suggests that the zonal scale of the meanders of the TgWC axis is consistent with the scale of the maximum growth wavelength of the baroclinic instability, especially in summer and autumn.

Furthermore, using JCOPE-T DA outputs, we estimated the zonal length scale of meanders in the deeper layer (50 m and 150 m) and compared the zonal difference of the peak in the deeper layer to that at the surface, D_p (Fig. 10). Here, from a statistical point of view, we used the average of L_p as the wavelength of meanders; L_p (1,1) is the difference in zonal distance around peaks of the axis between the first and second peaks at the surface,

L_p (1,2) is that between the second and third peaks at the surface, L_p (2,1) is the difference in zonal distance around peaks of the axis between the first and second peaks at deeper depths, and L_p (2,2) is that between the second and third peaks at deeper depths (Fig. 10a). The result indicates that, at both 50 m and 100 m, many meanders have zonal scales several times longer than the deformation radius (Fig. 10b and c, respectively). Furthermore, D_p is larger at 150 m than at 50 m, suggesting that the peak of the meander tends to precede with increasing depth (Fig. 10d and e). It is also indicated that the phase of the peak at 150 m is 1/4 wavelength ahead of that at the surface (Fig. 10e).

3.4 Instabilities suggested from the JCOPE-T DA outputs

The results mentioned above (Figs. 9 and 10) suggest the possibility of baroclinic instability in the eastern part of the Tsugaru Strait. Thus, to test whether necessary conditions of the instabilities, including baroclinic instability, can actually be satisfied there, we focused



on a case during July 26–27, 2019, using JCOPE-T DA output (including the period shown in Fig. 10a) as an example. In this duration, the TgWC at the surface flows at $\sim 41.6^\circ$ N (Fig. 11a). In contrast, the velocity maximum at 150 m shows meandering, that is, a convex structure is observed to the south at $141.20\text{--}141.4^\circ$ E (Fig. 11a). Thus, the positive field of the relative vorticity ($-U_y$; the first term on the right-hand side of Eq. 3) at 150 m is located beneath the eastward jet at the surface. Relative vorticity along the axis of the TgWC shows a slanted core of a positive (negative) region from $\sim 141.15^\circ$ E ($\sim 141.45^\circ$ E) to $\sim 141.4^\circ$ E ($\sim 141.5^\circ$ E) from the surface to the bottom, suggesting a slanted trough (crest) of the meander (Fig. 11b). In the region of $141.35\text{--}141.45^\circ$ E, divergence of the horizontal velocity, defined by the temporal mean of $\partial u/\partial x + \partial v/\partial y$, indicates a negative value (i.e., convergence) near the

bottom and a positive value (i.e., divergence) near the surface, suggesting upward velocity at this longitude (Fig. 11b). These results are consistent with the structure of the baroclinic instability.

The north–south derivation of the potential vorticity, Q_y (zonal mean between $141.3\text{--}141.4^\circ$ E), changes its sign in the north–south direction at $41.55\text{--}41.6^\circ$ N above 100 m and at $41.65\text{--}41.7^\circ$ N from the bottom to the surface, where vertical shear, U_z , is small ($< 0.005\text{ s}^{-1}$) (Fig. 11c). This situation can satisfy the necessary condition of instability [e.g., condition (a) in Sect. 8.4.2 of Holton (2004); condition (i) in Sect. 6.4.3 of Vallis (2006)]. Moreover, in the region of $41.6\text{--}41.65^\circ$ N, the sign of Q_y is positive under positive vertical shear (Fig. 11c). Due to the variation in the bathymetry in the zonal direction, although it is difficult to determine the lower boundary (e.g., Fig. 11b),

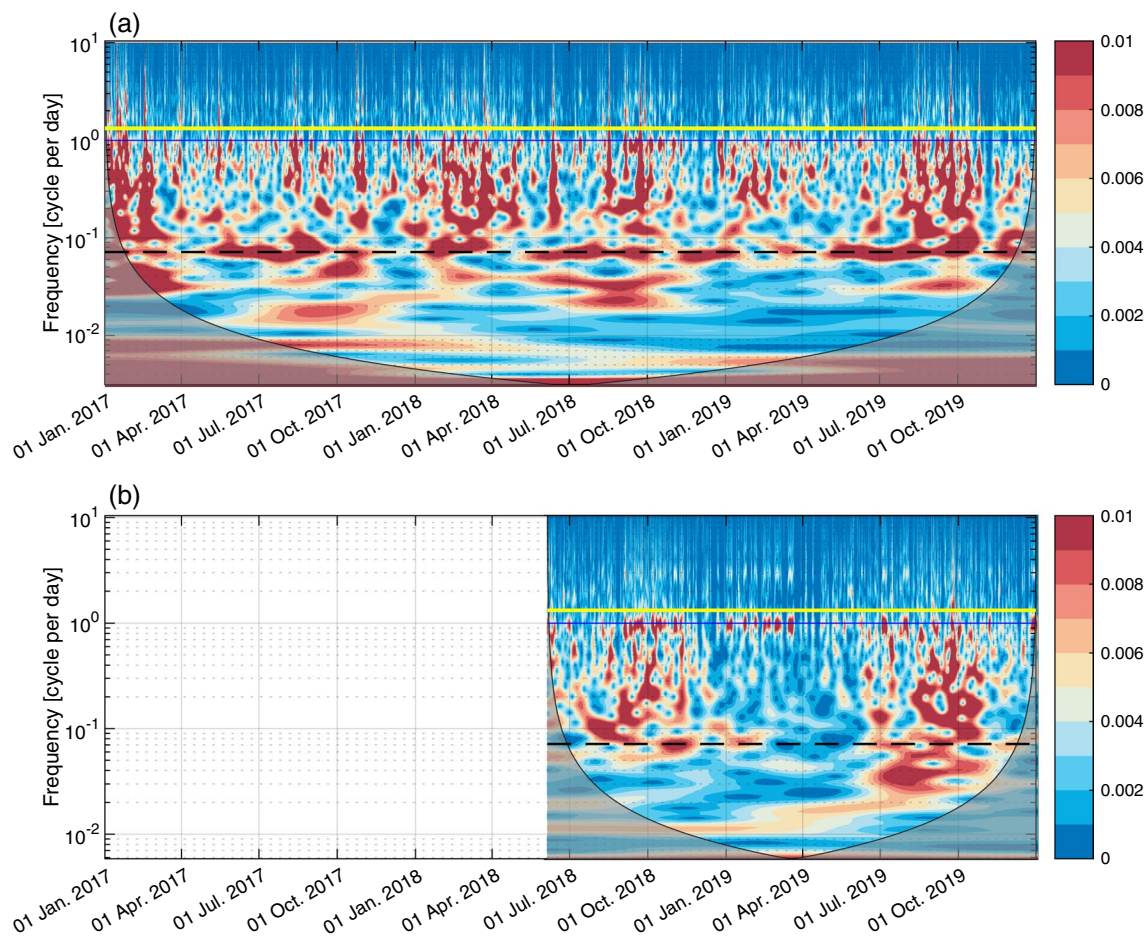
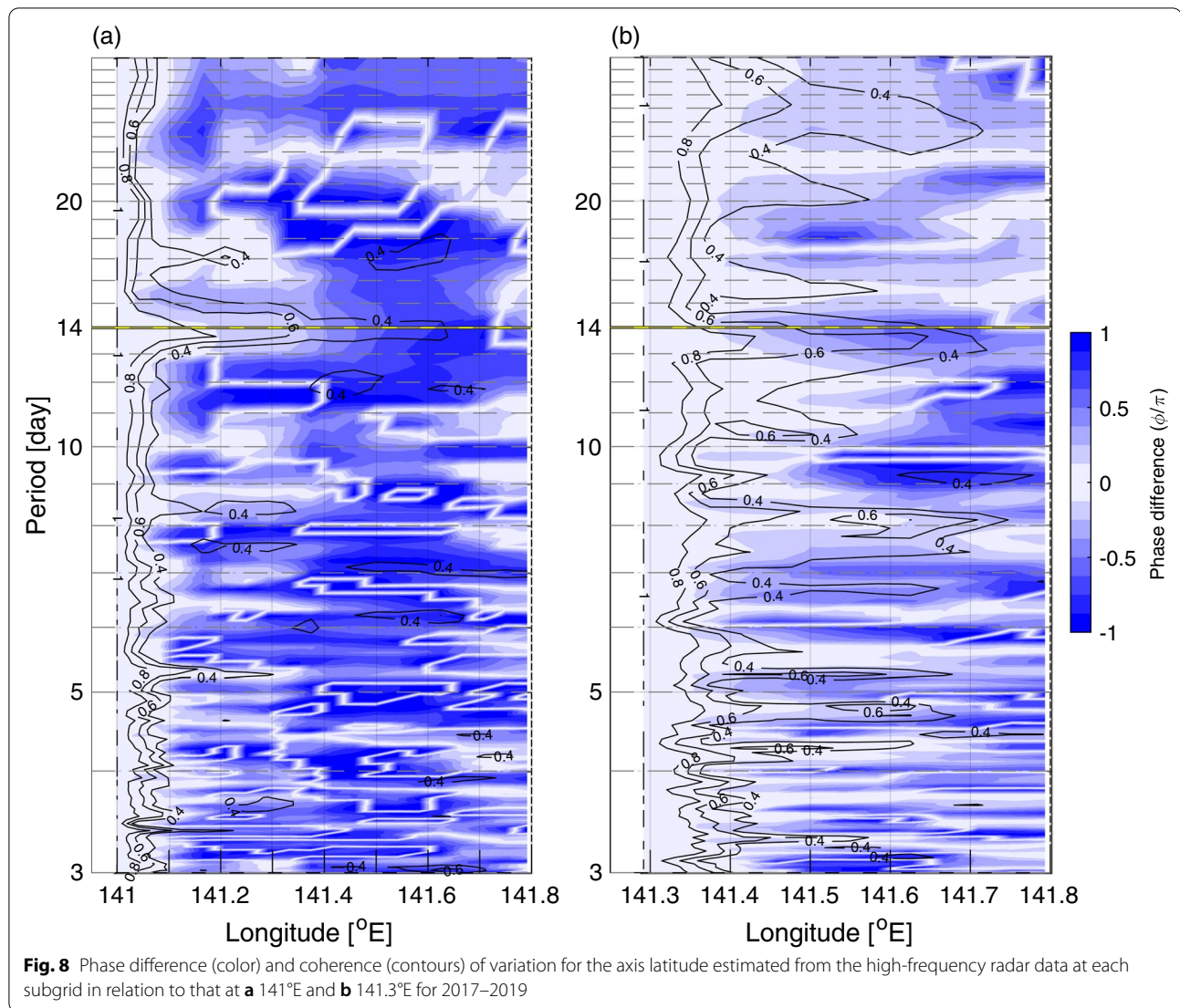


Fig. 7 Wavelet transform of the axis of the Tsugaru Warm Current at 141.3°E calculated from **a** the high-frequency radar data and **b** the JCOPE-T DA data. The yellow line indicates the inertial frequency at 41.5°N, 1.26 cycles per day (periods of 0.75 days). The blue and black lines denote 1 and 0.07 cycles per day (periods of 1 and 14 days), respectively

the necessary condition of the baroclinic instability [e.g., condition (b) in Sect. 8.4.2 of Holton (2004); condition (iii) in Sect. 6.4.3 of Vallis (2006)] could be satisfied in the eastern part of the Tsugaru Strait.

As it is shown that the necessary conditions of the instabilities can be satisfied in the example case, we also computed energy conversion rates for both potential and kinetic energy for each season (3 months) from the JCOPE-T DA data for 2019 (Figs. 12 and Additional file 1: Fig. S5). These results suggest that substantial mean field to eddy energy conversion of potential energy (i.e., baroclinic instability) occurs near the front in the strait (41.6° N, 141.0–141.3° E) at depths shallower than 100 m and in the region shallower than 150 m east of Cape Shiriya during summer and autumn (Fig. 12). Marked energy conversion of kinetic energy from the mean field to the eddy is also suggested at approximately 141.0° E and 141.5° E

(above the spur of Shiriya) for all seasons (Fig. 12) and south of the front near the surface (41.5–41.6° N, < 100 m; Additional file 1: Fig. S5). It should be noted, however, that the c'_p term is superior to the c'_k term near the surface (< 100 m) at approximately 141.3°E in summer (Fig. 12) and autumn at 41.6° N (Additional file 1: Fig. S5). Furthermore, although the density field over the topography of Shiriya (~ 141.5° E) in these seasons also indicates the possibility of a hydraulic jump, it is worth noting that c'_p is also large in areas more distant from the topography (~ 141.3° E, and ~ 142° E; Fig. 12). It is also worth noting that eddy to mean energy conversion of kinetic energy is suggested north of 41.6° N during summer and autumn (Additional file 1: Fig. S5). Thus, these energy conversions of kinetic energy (such as interactions between eddies frequently excited by the intense tide and mean flow; e.g., Wada et al. 2012, see also Sect. 4.3) would also affect the variation in the TgWC axis in addition to baroclinic instability.



4 Discussion

4.1 Propagation speed estimation of the meanders observed from the HFR

Based on the JCOPE-T DA outputs, the possibility of baroclinic instability is suggested in the region distanced from the characteristic topography, as mentioned above (Figs. 10, 11, 12). Thus, we examined the propagation speed of the meanders observed by the HFR following baroclinic instability theory. As the dominant scale of the meanders in the zonal direction is ~ 35 km in summer (Fig. 9), if we consider the 14-day period variation to have this zonal scale, the propagation speed is estimated to be ~ 0.03 m s $^{-1}$. This value is much smaller than the mean velocity, even at lower depths ($U_2 \sim 0.11$ m s $^{-1}$ m for geostrophic velocity and $U_2 \sim 0.15$ m s $^{-1}$ for the JCOPE-T DA output, Additional file 1: Fig. S1). Therefore, we focused

the timescale from 1.3 to 3 days, assuming that the timescale of dominant meanders (Fig. 9) would be distinct from diurnal tides. We also focused on two seasons, summer and autumn, since the zonal scale of the meanders detected by the HFR agreed well with the wavelength of the maximum growth rate for these seasons (Fig. 9).

To examine the relationship between the variations in each subregion, we calculated the lagged correlation of the time series of the axis latitude obtained from the HFR between the reference subregion and the other subregions, as mentioned in Sect. 2.4. Here, we employed subregion R3 as the reference region where the perturbation was expected to be generated after testing other cases from R1 to R3. Examples of bandpassed time series and lagged correlation are shown in Additional file 1: Fig. S6a and S6b, respectively. We plotted the lag time of the correlation peaks (shown by triangles in Additional file 1:

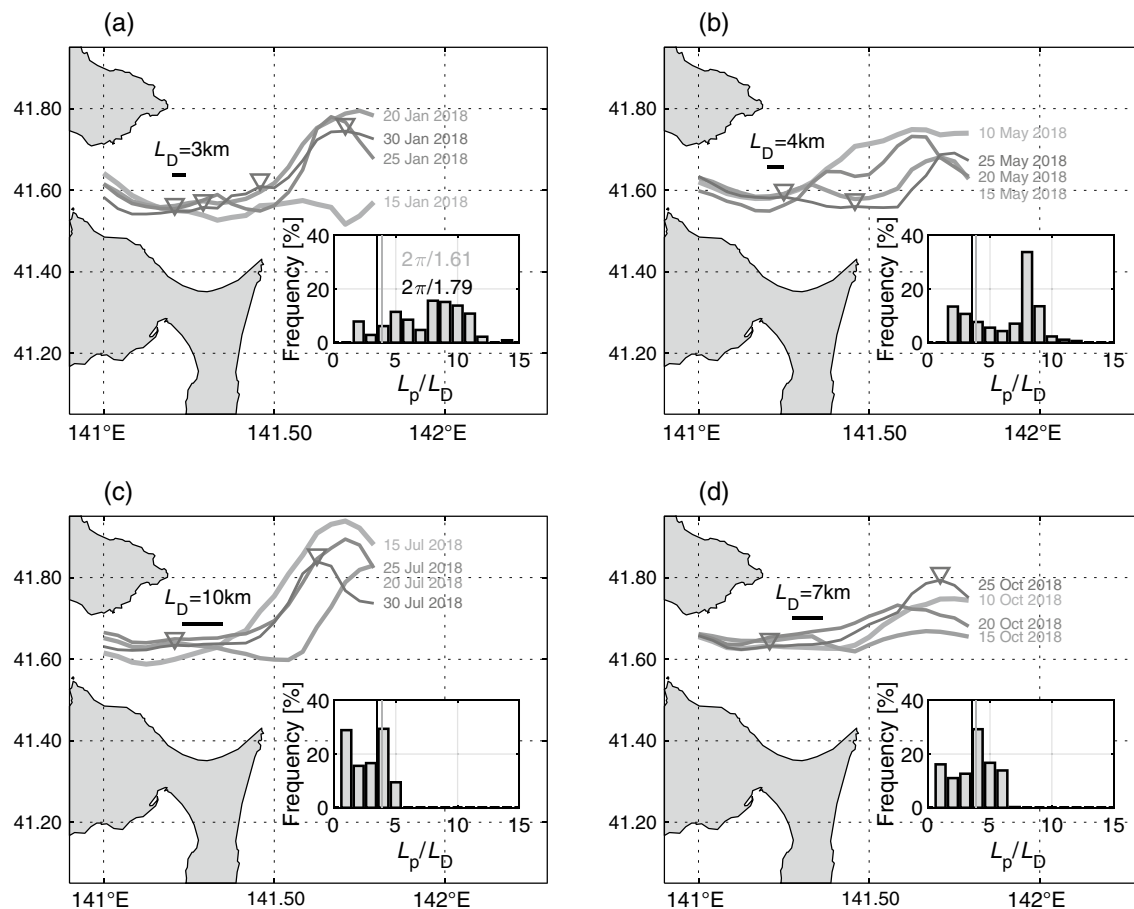


Fig. 9 Examples of shorter-term variation in the axis of the Tsugaru Warm Current estimated from the high-frequency radar during **a** winter, **b** spring, **c** summer, and **d** autumn. The thick–light (thin–dark) lines denote earlier (later) dates. The frequency distribution of the ratio of the zonal scale of adjacent meandering peaks (L_p) to the internal deformation radius (L_D) for each season is shown in the subpanels

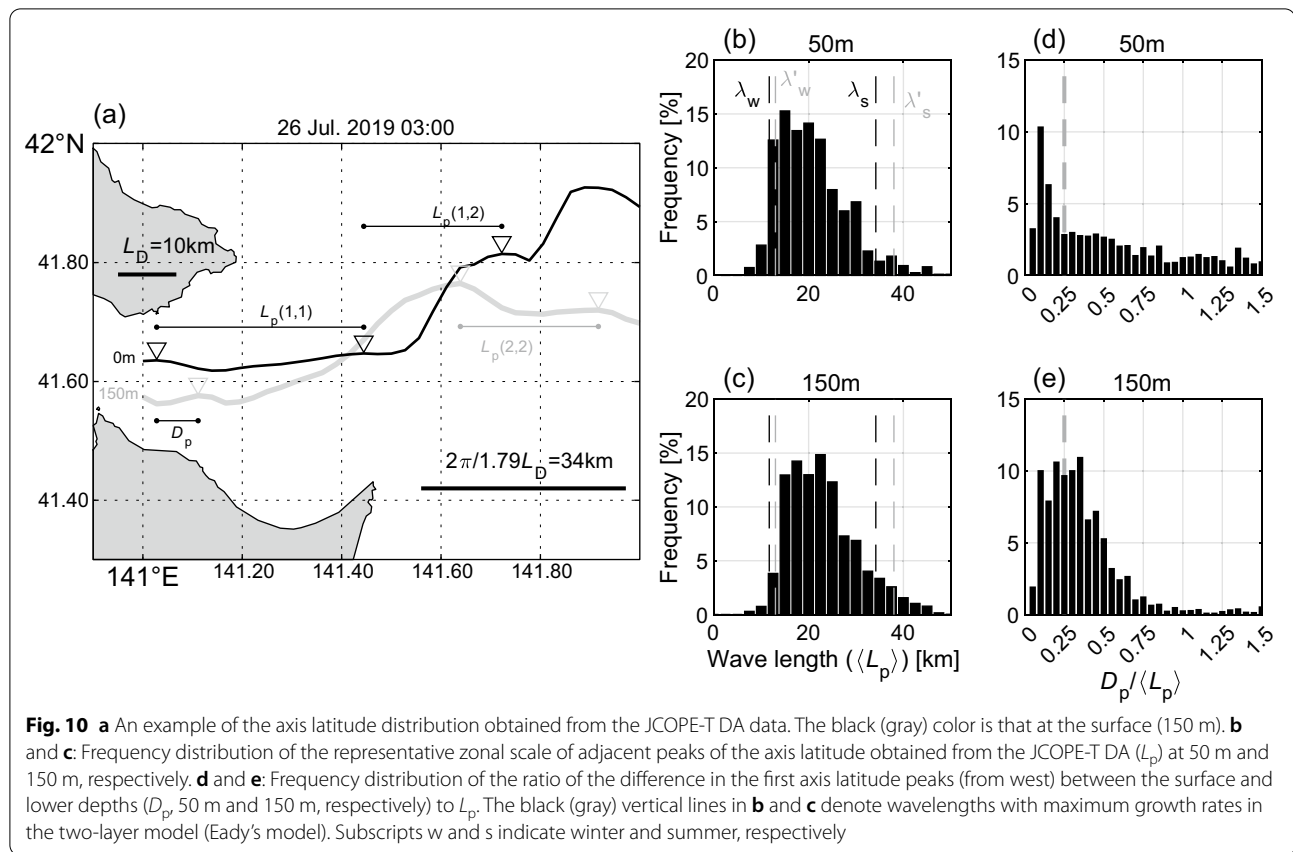
Fig. S6b) for the positive range (i.e., $\text{lag} > 0$ in Additional file 1: Fig. S6b) against the distance from the reference subregion for each season and each year (Fig. 13). We regarded the slope of the symbol plots in Fig. 13 as the propagation speed of the axis meander observed by the HFR.

To calculate the theoretical propagation speed as mentioned in Sect. 2.4, we also estimated the timescale of advection owing to the upper- and lower-layer velocities (U_1 and U_2 , respectively) in two ways: the mean geostrophic velocity (gray broken lines in Fig. 13) and the JCOPE-T DA data (Additional file 1: Fig. S1) (blue broken lines in Fig. 13). It should be noted that because the westward velocity south of the axis, especially in the upper layer (Figs. 3, 4, and 5), is excluded, U_1 is greater than another mean velocity for 41.5–41.7°N in Additional file 1: Fig. S1. We used the following baroclinic instability wavelengths for each season: 34 km (summer) and 26 km (autumn). These wavelengths satisfy the instability

condition of the two-layer model (e.g., Eq. 7.11.10 of Pedlosky 1987).

Then, the propagation speed of the baroclinic instability ~ 0.33 to ~ 0.35 m s^{−1} is consistent with that of the slope of the plots estimated from observations in summer (Fig. 13a). In autumn, the propagation speed appears to be similar to that of the two-layer model, especially for 2018 and 2019 in the region west of Cape Shiriya (Fig. 13b). Therefore, the propagation speed of the observed perturbation appears to agree with that of the baroclinic instability in the case of the two-layer model in summer and autumn. It should be noted that during the summer of 2017, there are no observations (Table 2) or outputs of JCOPE-T DA; thus, the difference in the propagation speed may be caused by the lack of velocity data.

Because a larger internal deformation radius than that in the present study has been reported for the area east of Cape Shiriya (i.e., the Pacific Ocean that is out of the HFR range) (Conlon 1982), the dominant zonal scale of



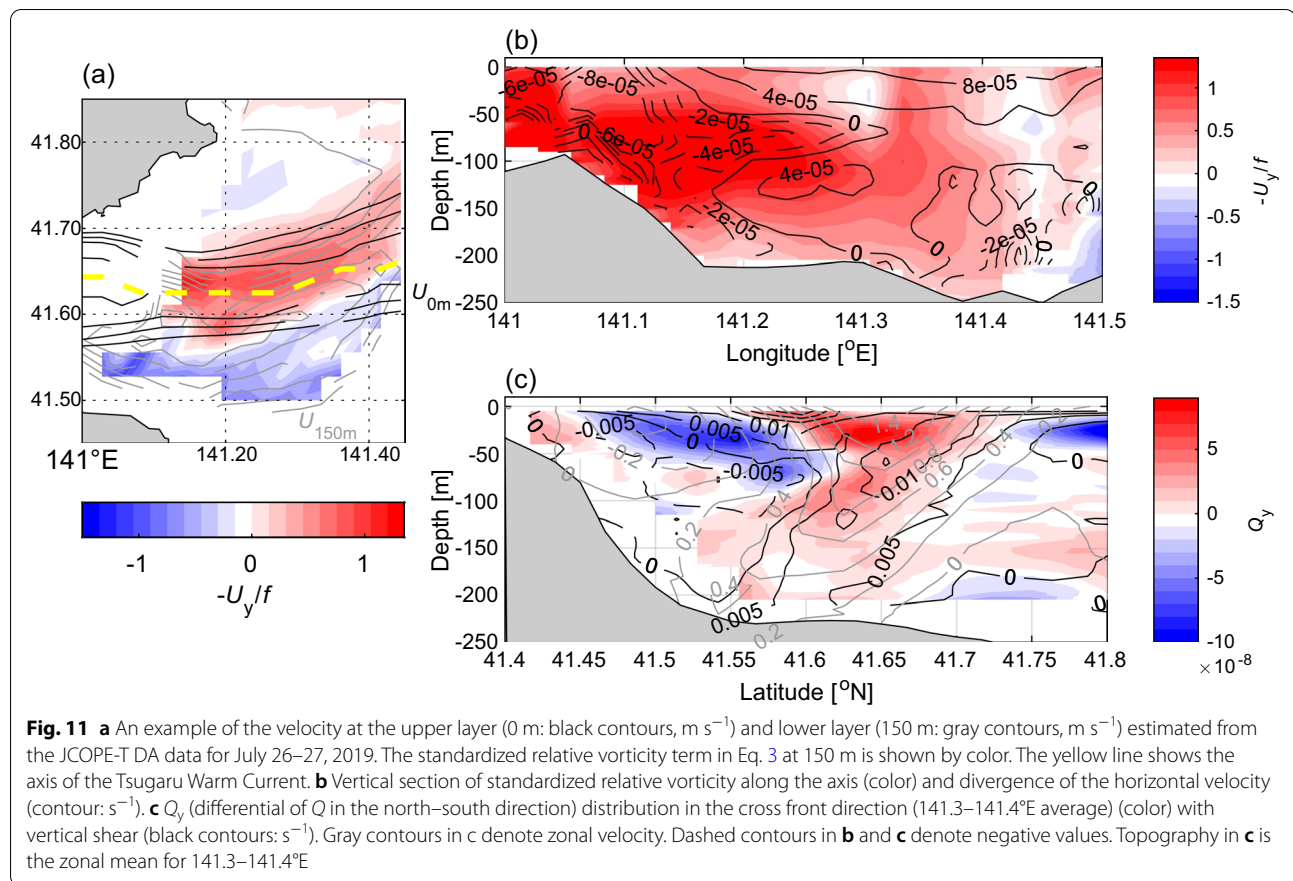
the meander may also become larger in this region. Conlon (1982) showed the internal deformation radius to be 18.4–23.2 km from July to September and 14.2–22.7 km from October to December based on the observational data obtained at 40.54° N, from ~142° E to ~144° E. Therefore, estimation of the length scale of the instability should still be addressed, especially east of Cape Shiriya. Outside of the strait, other subinertial frequency variations in the TgWC (from 10 days to one month) were also reported by Yasuda et al. (1988). The relationship of fluctuations with periods longer than 10 days was captured in this study (Fig. 7), and the previously reported variations will also be the subject of future work.

4.2 Seasonal variation in the wind effects on the several-day variation in the axis

In the present study, we found perturbations of the axis with timescales between 1 and 14 days, especially from July to September (Fig. 7). In these months, the local wind in the eastern part of the strait switches from easterly to westerly (K21). K21 also referred to the possibility that strengthening of the downfront (i.e., westerly) wind from the end of summer to early autumn could generate frontal variations and subsequent instabilities, including

baroclinic instability, as suggested by previous studies (e.g., Boccaletti et al. 2007; Yoshikawa et al. 2012; Thomas et al. 2013). Thus, we examined the seasonal wind influence on the variation in the TgWC axis using wind data at three capes, Shiriya, Esan, and Ōma (Fig. 14a).

First, we compared the variation in the latitude of the TgWC axis at each subgrid with the hourly averaged zonal wind (eastward positive) at each point for 2017–2019. Marked coherence is shown from 1.3 to 3 days (1.5, 2.0, 2.5, and 3.0 days, for example) in the region of 141.0–141.6° E for each case (Fig. 14b–d). Then, to examine the temporal variation, we also calculated wavelet coherence between the variation in the axis at each subgrid (Fig. 1c) and the mean wind for each point (i.e., Shiriya, Esan, and Ōma). Here, the longitudinal (statistical) average of the wavelet coherence (141.3–141.6° E) calculated from the axis variation at each subgrid is shown in Fig. 15a. Subsequently, we statistically averaged the coherence from 1.3 to 3 days to estimate the seasonal variation in the coherence (Fig. 15b). Relatively high coherence (>0.3, 30-day running mean) is shown from September to October, especially for 2018 (Fig. 15b). Then, each year average ($\langle C_w \rangle_{yr}$) was estimated using the 30-day running mean coherence from 2017 and 2019 (Fig. 15c).



A relatively large value of $\langle C_w \rangle_{yr} > 0.3$ is shown from September to October, when the zonal wind changes its sign from negative (i.e., easterly) to positive (westerly) (Fig. 15c). Thus, around September, the variation in zonal wind over the strait with a timescale of several days along the TgWC current is expected to be closely related to that of the TgWC axis. The coherence from December to the following February tends to be smaller than that in September despite the marked westerly wind (Fig. 15c) and its variance (Fig. 15d). Thus, the remarkable coherence in September is characteristic. This characteristic is consistent with the theory of the downfront wind. The processes due to the downfront wind can proceed with stratification in the eastern part of the Tsugaru Strait, as mentioned by previous studies (e.g., Boccaletti et al. 2007; Yoshikawa et al. 2012; Thomas et al. 2013), which may result in a situation similar to the two-layer model in the strait. More precise quantitative evaluation of both horizontal and vertical transport (such as Tanaka et al. 2021) of heat and materials should be addressed in the future in addition to evaluation of the wind effects. The elucidation of the material circulation process in the strait is important for commercial activities, such as fisheries, including the nearby aquaculture industry, as well as scientific

understanding, such as rapid acidification in the strait (Wakita et al. 2021).

4.3 Other issues to address

The impact of the characteristic topography in the strait on the instability is another issue to be considered. Although the topography in the Tsugaru Strait is complex, the northern part of the strait is open east to 141.2° E and the topography generally deepens toward the north at 141.2–141.5° E (Fig. 1c), which does not seem to match the stable configuration as it relates to the slope condition of the baroclinic instability (Fig. 1d of Blumsack & Gierasch 1972). However, the TgWC sometimes rises across the ridge in summer and autumn (Fig. 9c and d). Baroclinic flow that overrides topography can cause horizontal eddies downstream of the topography through stretching of the water column, subsequently affecting the pathway of the coastal current (e.g., Nakada et al. 2003; Igeta et al. 2017, 2021). Thus, this effect should also be re-examined from the perspective of the seasonal path change in the TgWC during the stratified season (e.g., gyre mode) in addition to the effect examined in K21. The path change may also be important from the perspective of balance of the frictional torque due to the

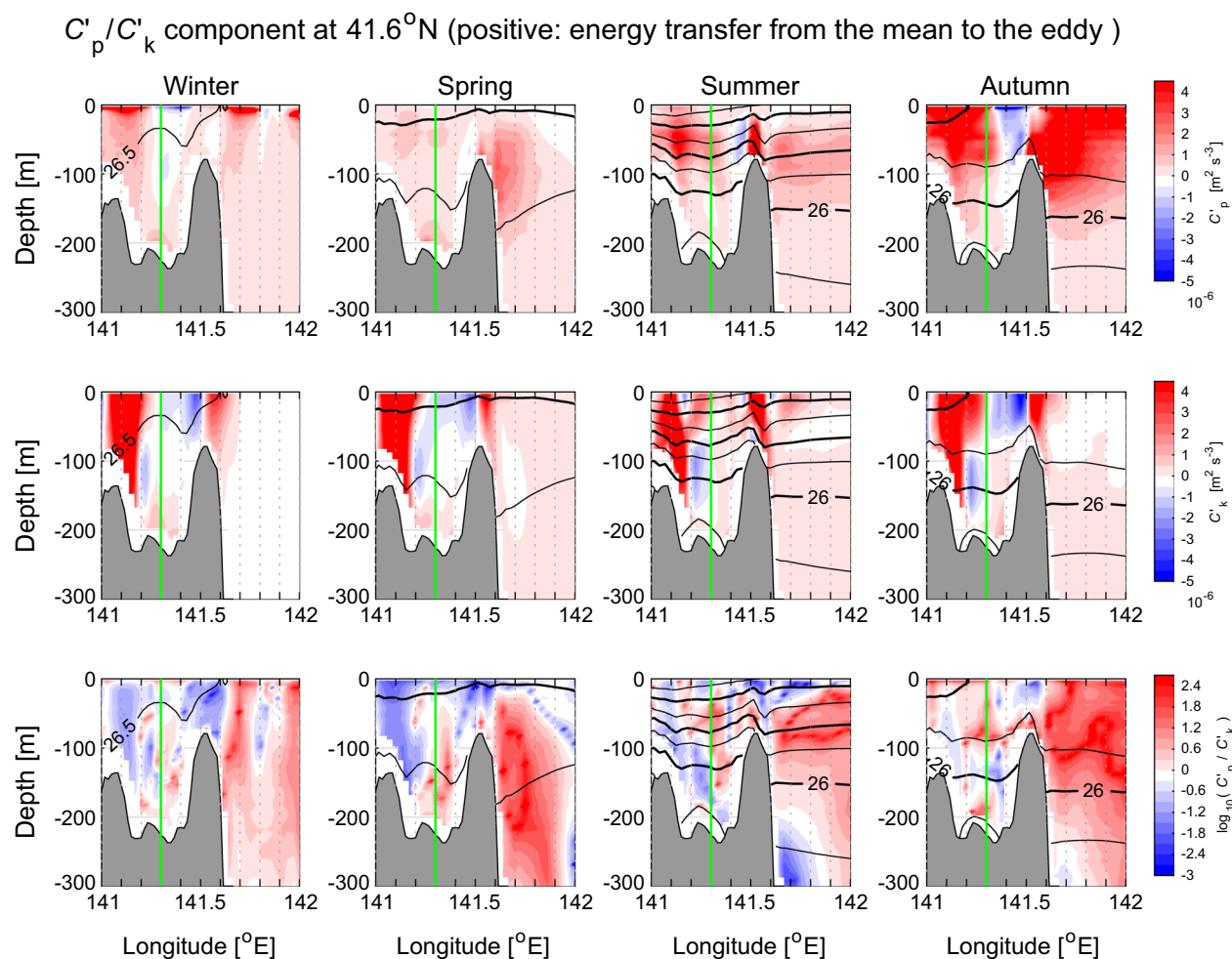


Fig. 12 Vertical distribution of the energy conversion rate calculated from the JCOPE-T DA data during 2019 (upper row: potential energy; middle row: kinetic energy) and their ratio (that of potential energy to that of kinetic energy, lower row) in each season at 41.6°N . Black contours denote the potential density anomaly, σ_θ . The green line denotes 141.3°E (see Additional file 1: Fig. S5)

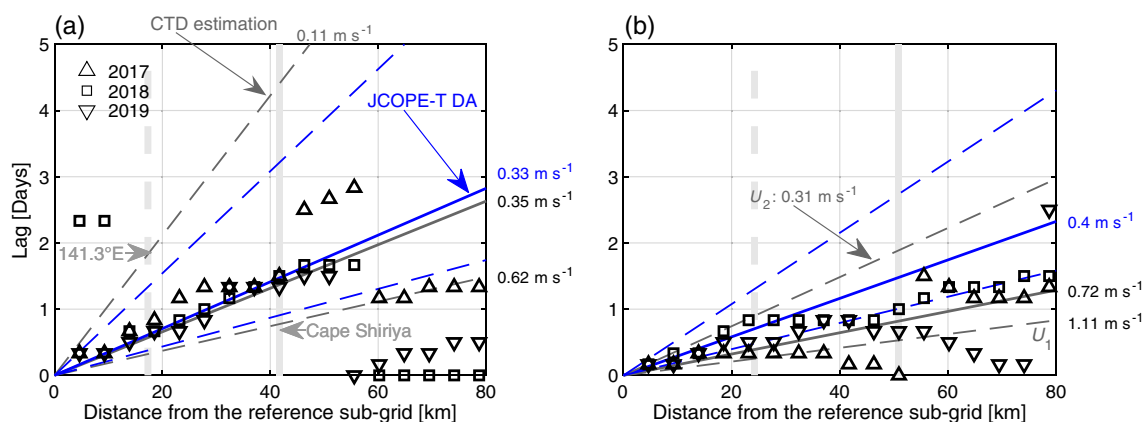
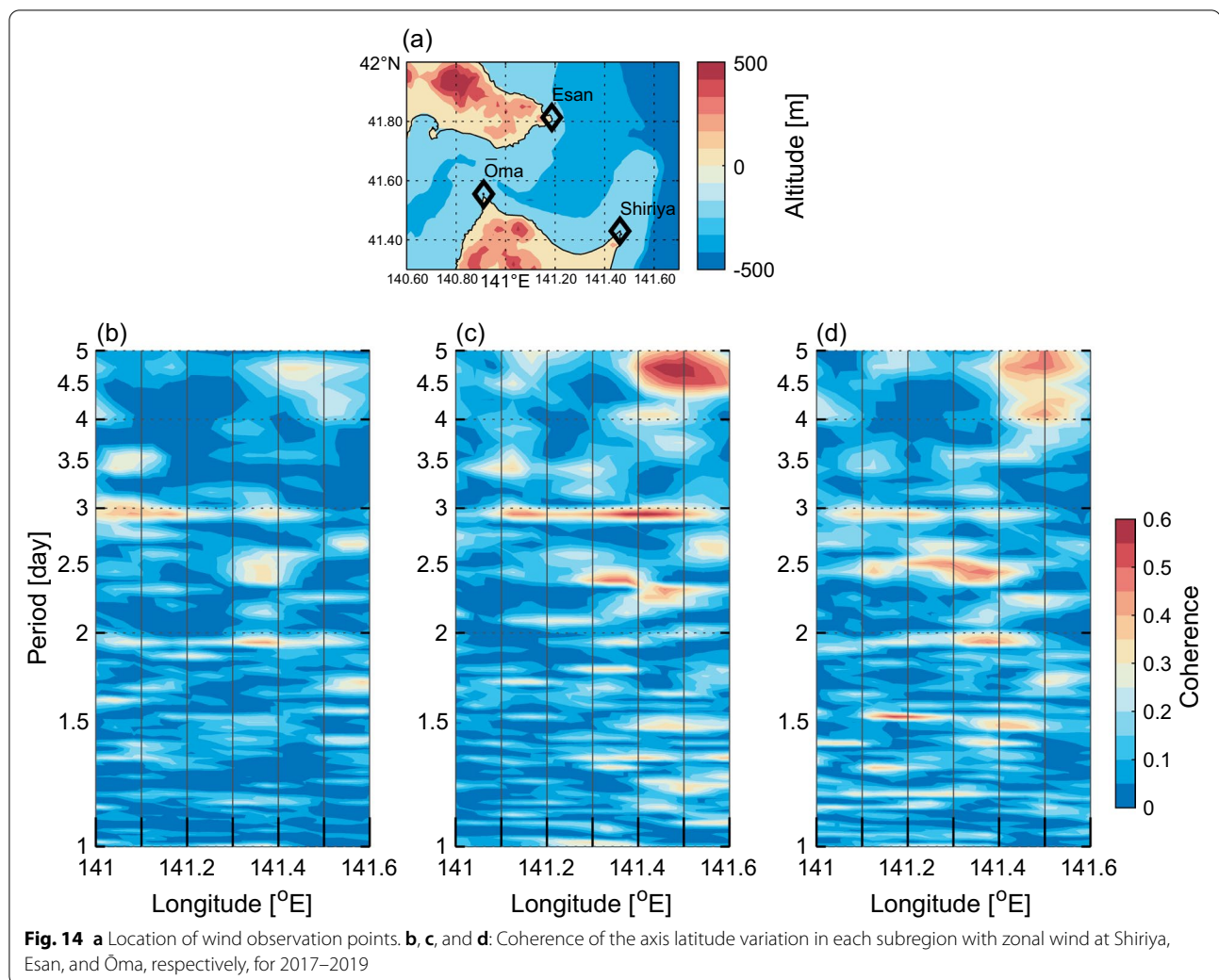


Fig. 13 Distance-lag plot calculated from the high-frequency radar data in **a** summer and **b** autumn



coastal boundary current system around Japan, such as the Kuroshio, TsWCs, and TgWC (Sasaki et al. 2014; Kida et al. 2016, 2020).

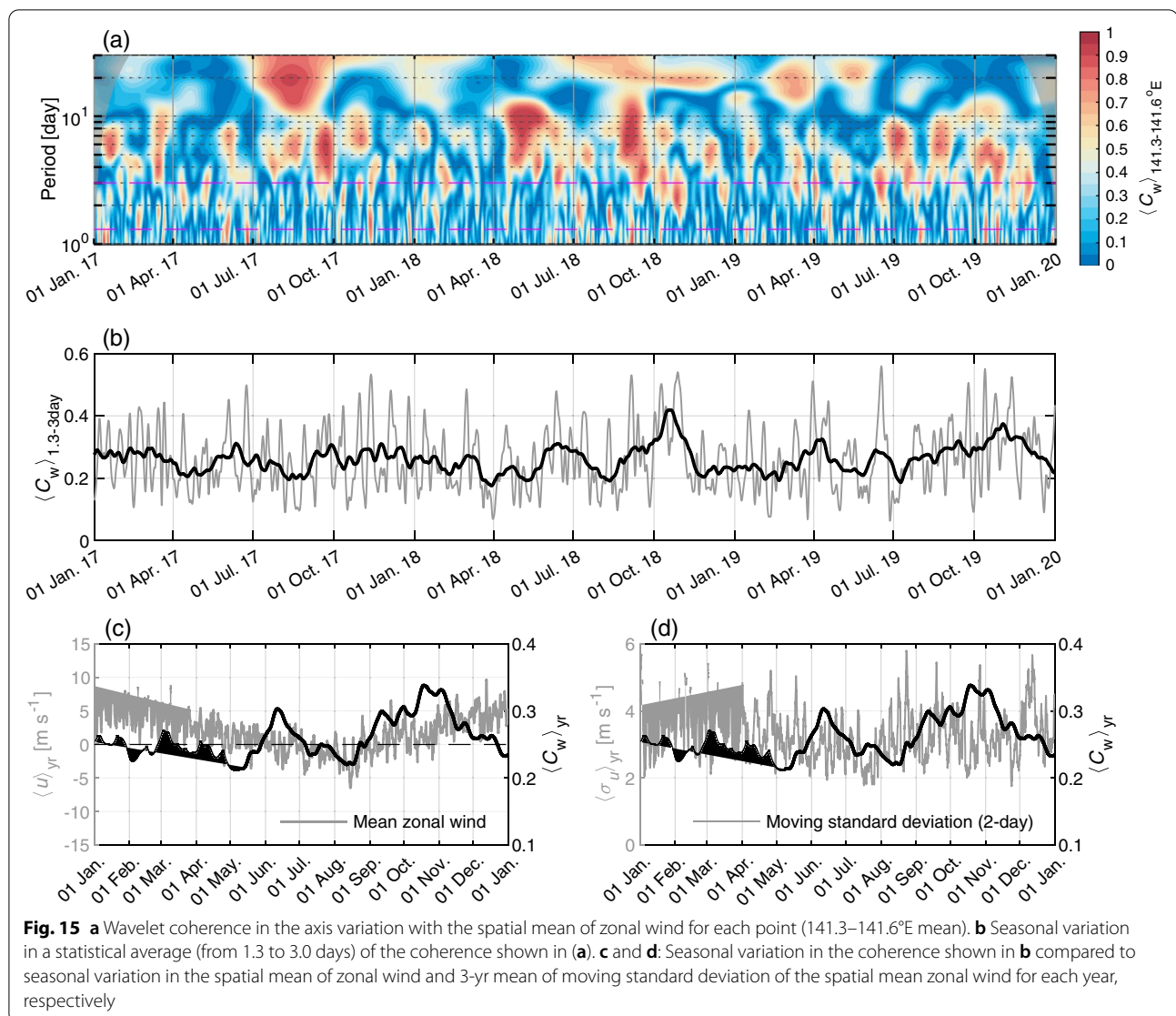
Moreover, Yasui et al. (2022) recently suggested that the TgWC tends to flow with an increase in inertia over the topography at Cape Shiriya, even in winter. Although wintertime stratification is weak in the strait and barotropic disturbance dominates (e.g., Figs. 2a e, 3a, e, and 12), confluence of the TgWC Water and Coastal Oyashio Water may form a baroclinic structure and disturbances. Thus, the relationship between the topography, baroclinicity, and path of the TgWC is also an issue to address in winter and early spring, together with the effect of barotropic shelf-trapped waves (e.g., Ohshima 1994). Furthermore, as shown in Fig. 12, the kinetic energy conversion from eddy to mean in the eastern part of the strait (141.2–141.4° E) could also be important for the variation in the TgWC axis in addition to that from the mean to eddy at ~141.2° E. Because remarkable eddies are

generated at approximately 141.0°E due to intense tides (e.g., Asano et al. 2020; Ishizaki et al. 2022), the effects of the advection of such eddies downstream (Wada et al. 2012) on the meandering of the TgWC should also be investigated.

5 Conclusions

In the present study, using data obtained from the HFR system and that from the JCOPE-T DA data assimilated model (Miyazawa et al. 2021) with high resolution (1/36°, hourly), we focused on the frontal variation along the axis of the TgWC that varies on a shorter-than-seasonal timescale in the eastern part of the Tsugaru Strait. Variations between 1 and 14 days, especially during summer and autumn, are seen in the HFR data and are also represented by the JCOPE-T DA.

The seasonal variation in the ~14-day coherence is consistent with a previous study focusing on tides at approximately 141.0°E (Tanno et al. 2005), and the



phase change downstream (to the east) is shown based on the HFR data. The zonal scale of the TgWC axis meanders estimated from the HFR and the vertical structure of the meanders estimated from the JCOPE-T DA are consistent with the baroclinic instability. The propagation speed of the 1.3–3-day variation in the axis estimated from the HFR agrees well with that calculated from the two-layer baroclinic instability theory from summer to autumn. Moreover, based on the JCOPE-T DA outputs, it is indicated that potential energy conversion from the mean to the eddy occurs at approximately 141.3° E and east of Cape Shiriya in summer and autumn, in addition to kinetic energy conversion near the outlet of the channel (~141.0° E). These results suggest baroclinic instability in the eastern part

of the Tsugaru Strait that is distanced from some of the characteristic topographies, especially from summer to autumn, as well as other instabilities near these topographies. This baroclinic instability with a several-day timescale during summer and autumn may be caused by the seasonal downfront (westerly) wind in the strait and subsequent instabilities near the surface (Boccaletti et al. 2007; Yoshikawa et al. 2012; Thomas et al. 2013).

In conclusion, this study reveals part of the subinertial frequency variation process in the eastern Tsugaru Strait related to meanders by combining shipboard observations and high-resolution HFR remote sensing with high-resolution model output. The variations can affect the north–south water mass mixing and the stratification in the eastern part of the strait. The

findings of this study and the extension of the methodology can also be applied to the improvement in K21 using information about internal structures within and outside the strait provided by the JCOPE-T DA.

Abbreviations

CTD: Conductivity–temperature–depth (observation); cpd: Cycles per day; HFR: High-frequency radar; JAMSTEC: Japan Agency for Marine–Earth Science and Technology; JCOPE-T DA: Japan Coastal Ocean Predictability Experiment, tide enabled, data assimilated version; K21: Kaneko et al. (2021); MIO: Mutsu Institute for Oceanography; MORSETS: MIO Ocean Radar data Site for the Eastern Tsugaru Strait; R/V: Research vessel; SADCP: Acoustic Doppler current profiler mounted on some ships; SE: Shiriya–Esan (line); T/S: Training ship; TgWC: Tsugaru Warm Current; TsWC: Tsushima Warm Current.

Supplementary Information

The online version contains supplementary material available at <https://doi.org/10.1186/s40645-022-00509-z>.

Additional file 1. Fig. S1: Time series of zonal velocity estimated by JCOPE-T DA. a Upper layer (vertical mean) velocity U_1 , b lower-layer (vertical mean) velocity U_2 , and c meridional mean of U_1 and U_2 . The solid line in c denotes the meridional mean for 41.5–41.7°N. The dashed lines in c for summer and autumn correspond to the meridional mean for the range represented by the dashed lines in a and b. **Fig. S2:** Time series of variation in the bandpass-filtered axis latitude at 141.08°E (between 12 and 15 days) from 2017 to 2019 (black line). The gray line denotes the tidal variation in the Mf component estimated from sea level data at the Mutsu Institute for Oceanography through harmonic analysis. Solid (open) circles show the timing of a new (full) moon. **Fig. S3:** Same as Fig. S2, but the gray line denotes the tidal variation in the K_1 and O_1 components estimated from sea level data at the Mutsu Institute for Oceanography through harmonic analysis. **Fig. S4:** a Phase difference of wavelet cross spectrum of latitude variation around the axis at each subgrid in relation to the Mf tide component (color). The contours denote their wavelet coherence. b–e: Longitudinal distribution of spectrum ratio $R_{F-P(1,2)}$ defined by Eq. 2 for each season. **Fig. S5:** Same as Fig. 12 but along 141.3°E. **Fig. S6:** a Example of the time series of bandpass-filtered latitude variation in the axis of the Tsugaru Warm Current calculated from the high-frequency radar data in 2017. The cutoff timescales are 1.3 and 3.0 days. b Examples of the lagged correlation (r) of various subregions with respect to the reference subregion (R1). Triangles show peaks in the lagged correlation. Thin lines denote the 95% confidence interval.

Acknowledgements

The authors acknowledge the assistance of the staff at the Mutsu Institute for Oceanography and the Research Institute for Global Change of JAMSTEC. We also acknowledge the assistance of the captains and crews of T/S *Ushio-Maru*, *Oshoro-Maru*, and R/V *Wakataka-Maru* for their cooperation during sample collection and hydrographic measurement for cruises during 2009–2019. We appreciate the work of the technical support staff from Marine Work Japan. We also thank T. Yasui, T. Hashimukai, T. Nakayama, and S. In for their helpful comments.

Author contributions

HK conceptualized the present study, performed analysis of the data obtained from the HFR and shipboard observations, created the figures, and wrote the manuscript based on comments from all authors. HK, TT, HA, MW, KS, and TO devised the observation plan and engaged in the collection of in situ data together with ST. SW and KS were involved in the planning and installation of the HFR, and they facilitated and supervised the continuous observation of the HFR. YM is a developer and established the JCOPE-T DA system. YS was responsible for the management and retention of the HFR data. All authors contributed to discussions of the results and commented on the manuscript. All authors read and approved the final manuscript.

Funding

This study was supported by the research and assessment program for fisheries resources of the Fisheries Agency of Japan.

Availability of data and materials

The datasets of surface velocity obtained from the HFR analyzed for this study are distributed through the Mutsu Institute for Oceanography, JAMSTEC (<https://www.godac.jamstec.go.jp/morsets/e/top/>). The JCOPE-T DA data are distributed by JAMSTEC from <http://www.jamstec.go.jp/apl/j/database/>. The wind speed data are available from the Japan Oceanographic Data Center (<https://jdoss1.jodc.go.jp/vpage/wave.html>). Topographic data were provided by the NOAA National Geophysical Data Center (<https://www.ngdc.noaa.gov/mgg/global/relief/ETOPO1/>). The other data analyzed in this study are available from the corresponding author upon reasonable request.

Declarations

Competing interests

The authors declare that they have no known competing interests.

Author details

¹Mutsu Institute for Oceanography, Research Institute for Global Change, Japan Agency for Marine–Earth Science and Technology (JAMSTEC), 690 Kitasekine, Sekine, Mutsu, Aomori 035-0022, Japan. ²Fisheries Resources Institute, Japan Fisheries Research and Education Agency, 3-27-5 Shinhamacho, Shiogama, Miyagi 985-0001, Japan. ³Faculty of Fisheries Sciences, Hokkaido University, 3-1-1 Minato-cho, Hakodate, Hokkaido 041-8611, Japan. ⁴Application Laboratory, Research Institute for Value-Added-Information Generation, Japan Agency for Marine–Earth Science and Technology (JAMSTEC), 3173-25, Showa-machi, Kanazawa-ku, Yokohama, Kanagawa 236-0001, Japan.

Received: 24 June 2021 Accepted: 21 September 2022

Published online: 15 October 2022

References

- Abe H, Sasaki K, Yasui T, Wakita M (2020) Observation of Tsugaru warm current by high frequency radar and preliminary result for its prediction. *Kaiyo Mon* 52:312–316 (in Japanese with English abstract)
- Amante C, Eakins BW (2009) ETOPO1 1 Arc-minute global relief model: procedures, data sources and analysis. In: NOAA Technical Memorandum NESDIS NGDC-24. National Geophysical Data Center, NOAA. Doi:<https://doi.org/10.7289/V5C8276M> [Accessed on 23 June 2021]
- Asano R, Isoda Y, Kobayashi N, Nakamura T, Itoh K (2020) Vertical circulation induced by negative shear flow at the downside of Oomazaki in the Tsugaru Strait. *Bull Fish Sci Hokkaido Univ* 70(1):63–76. <https://doi.org/10.14943/bull.fish.70.1.63> (in Japanese with English abstract)
- Blumsack SL, Gierasch PJ (1972) Mars: the effects of topography on baroclinic instability. *J Atmos Sci* 29:1081–1089. [https://doi.org/10.1175/1520-0469\(1972\)029%3c1081:MTEOTO%3e2.0.CO;2](https://doi.org/10.1175/1520-0469(1972)029%3c1081:MTEOTO%3e2.0.CO;2)
- Boccaletti G, Ferrari R, Fox-Kemper B (2007) Mixed layer instabilities and restratification. *J Phys Oceanogr* 37:2228–2250. <https://doi.org/10.1175/JPO3101.1>
- Brooks DA, Bane JM (1981) Gulf-stream fluctuations and meanders over the Onslow Bay upper continental-slope. *J Phys Oceanogr* 11:247–256. [https://doi.org/10.1175/1520-0485\(1981\)011%3c0247:GSFAMO%3e2.0.CO;2](https://doi.org/10.1175/1520-0485(1981)011%3c0247:GSFAMO%3e2.0.CO;2)
- Brooks IH, Niiler PP (1977) Energetics of Florida current. *J Mar Res* 35:163–191
- Charney JG, Stern ME (1962) On the stability of internal baroclinic jets in a rotating atmosphere. *J Atmos Sci* 19:159–172. [https://doi.org/10.1175/1520-0469\(1962\)019%3c0159:OTSOIB%3e2.0.CO;2](https://doi.org/10.1175/1520-0469(1962)019%3c0159:OTSOIB%3e2.0.CO;2)
- Conlon DM (1982) On the outflow modes of the Tsugaru Warm Current. *La Mer* 20:60–64
- Dewar WK, Bane JM (1989) Gulf-stream dynamics. part II: eddy energetics at 73°W. *J Phys Oceanogr* 19:1574–1587. [https://doi.org/10.1175/1520-0485\(1989\)019%3c1574:GSDPIE%3e2.0.CO;2](https://doi.org/10.1175/1520-0485(1989)019%3c1574:GSDPIE%3e2.0.CO;2)
- Eady ET (1949) Long waves and cyclone waves. *Tellus* 1:33–52. <https://doi.org/10.1111/j.2153-3490.1949.tb01265.x>

- Ebuchi N, Fukamachi Y, Ohshima KI, Wakatsuchi M (2009) Subinertial and seasonal variations in the Soya Warm Current revealed by HF ocean radars, coastal tide gauges, and bottom-mounted ADCP. *J Oceanogr* 65:31–43. <https://doi.org/10.1007/s10872-009-0003-2>
- Emery WJ, Thomson RE (eds) (2001) Data analysis methods in physical oceanography, 1st edn. Elsevier Science, New York, p 654
- Gill AE (1982) Atmosphere-ocean dynamics. Academic Press, San Diego
- Hanawa K, Mitsudera H (1987) Variation of water system distribution in the Sanriku coastal area. *J Oceanogr Soc Jpn* 42:435–446. <https://doi.org/10.1007/BF02110194>
- Holton RJ (2004) An introduction to dynamic meteorology, 4th edn. Academic Press, p 553
- Igeta Y, Yankovsky A, Fukudome K, Ikeda S, Okei N, Ayukawa K, Kaneda A, Watanabe T (2017) Transition of the Tsushima Warm Current path observed over Toyama Trough Japan. *J Phys Oceanogr*. <https://doi.org/10.1175/JPO-D-17-0027.1>
- Igeta Y, Kuga M, Yankovsky A, Wagawa T, Fukudome K, Kaneda A, Ikeda S, Tsuji T, Hirose N (2021) Effect of a current trapped by a continental slope on the pathway of a coastal current crossing Toyama Trough, Japan. *J Oceanogr* 77:685–701. <https://doi.org/10.1007/s10872-021-00601-w>
- Ishizaki Y, Isoda Y, Taya K, Kobayashi N (2022) Long-lived Clockwise Topographic Separation Vortices with Strong Vertical Circulation at the Eastern Outlet of the Tsugaru Strait. *Bull Coastal Oceanogr* (in Japanese with English abstract). <https://doi.org/10.32142/engankaiyo.2022.9.001>
- Isobe A (1999) On the origin of the Tsushima Warm Current and its seasonality. *Cont Shelf Res* 19:117–133. [https://doi.org/10.1016/S0278-4343\(98\)00065-X](https://doi.org/10.1016/S0278-4343(98)00065-X)
- Ito T, Togawa O, Onishi M, Isoda Y, Nakayama T, Shimizu S, Kuroda H, Iwahashi M, Sato C (2003) Variation of velocity and volume transport of the Tsugaru Warm Current in the winter of 1999–2000. *Geophys Res Lett* 30(1–4):11. <https://doi.org/10.1029/2003GL017522>
- Itoh S, Sugimoto T (2008) Current variability of the Kuroshio near the separation point from the western boundary. *J Geophys Res* 113:C11020. <https://doi.org/10.1029/2007JC004682>
- Kaneko H, Sasaki K, Abe H, Tanaka T, Wakita M, Watanabe S, Okunishi T, Sato Y, Tatamisashi S (2021) The Role of an intense Jet in the Tsugaru Strait in the formation of the Outflow Gyre revealed using High-Frequency Radar Data. *Geophys Res Lett*. <https://doi.org/10.1029/2021GL092909>
- Kang D, Curchitser EN (2015) Energetics of Eddy-Mean Flow Interactions in the Gulf Stream Region. *J Phys Oceanogr* 45(4):1103–1120. <https://doi.org/10.1175/JPO-D-14-0200.1>
- Kawabe M (1982a) Branching of the Tsushima Current in the Japan Sea. Part I. Data analysis. *J Oceanogr Soc Japan* 38(2):95–107
- Kawabe M (1982b) Branching of the Tsushima Current in the Japan Sea. Part II. Numerical experiment. *J Oceanogr Soc Japan* 38(4):183–192
- Kida S, Qi B, Yang J, Lin X (2016) The annual cycle of the Japan Sea Throughflow. *J Phys Oceanogr* 46:23–39. <https://doi.org/10.1175/JPO-D-15-0075.1>
- Kida S, Takayama K, Sasaki YN, Matsuura H, Hirose N (2020) Increasing trend in Japan Sea Throughflow transport. *J Oceanogr*. <https://doi.org/10.1007/s10872-020-00563-5>
- Kimura S, Sugimoto T (1993) Short-period fluctuations in meander of the Kuroshio path off Cape Shiono-misaki. *J Geophys Res* 98(C2):2407–2418. <https://doi.org/10.1029/92JC02582>
- Kono T, Foreman M, Chandler P, Kashiwai M (2004) Coastal Oyashio south of Hokkaido, Japan. *J Phys Oceanogr* 34:1477–1494. [https://doi.org/10.1175/1520-0485\(2004\)034%3c1477:COSOHJ%3e2.0.CO;2](https://doi.org/10.1175/1520-0485(2004)034%3c1477:COSOHJ%3e2.0.CO;2)
- Kouketsu S, Yasuda I, Hiroe Y (2005) Observation of frontal waves and associated salinity minimum formation along the Kuroshio Extension. *J Geophys Res* 110:C08011. <https://doi.org/10.1029/2004JC002862>
- Kouketsu S, Yasuda I, Hiroe Y (2007) Three-dimensional structure of frontal waves and associated salinity minimum formation along the Kuroshio Extension. *J Phys Oceanogr* 37:644–656. <https://doi.org/10.1175/JPO3026.1>
- Kubokawa A (1991) On the behavior of outflows with low potential vorticity from a sea strait. *Tellus A* 43:168–176. <https://doi.org/10.1034/j.1600-0870.1991.t01-1-00007.x>
- Kuroda H, Isoda Y, Takeoka H, Kuma K, Honda S, Matsuura H, Saitoh Y, Takata H, Iwade S, Wagawa T, Kobayashi N (2012) Intrusion of the Oyashio water into the eastern mouth of Tsugaru Strait in early summer, 2003. *Cont Shelf Res* 32:36–46. <https://doi.org/10.1016/j.csr.2011.10.012>
- Lee TN, Atkinson LP (1983) Low-frequency current and temperature variability from gulf-stream frontal eddies and atmospheric forcing along the south-east United States outer continental-shelf. *J Geophys Res* 88(C8):4541–4567. <https://doi.org/10.1029/JC088iC08p04541>
- Matsuura H, Isoda Y (2020) Pseudo-fortnightly variation produced by interaction between passage-flow and diurnal tidal currents in the Tsugaru Strait. *Bull Fish Sci Hokkaido Univ* 70(1):13–23. <https://doi.org/10.14943/bull.fish.70.1.13>
- Matsuura H, Isoda Y, Kuroda H, Kuma K, Saitoh Y, Kobayashi N, Aiki T, Wagawa T, Yabe I, Hoshiba Y (2007) Water mass modification process of the passage-flow waters through the Tsugaru Strait. *Umi Sora* 83:21–35 (in Japanese with English abstract)
- Miyazawa Y, Varlamov SM, Miyama T, Kurihara Y, Murakami H, Kachi M (2021) A Nowcast/forecast system for Japan's coasts using daily assimilation of remote sensing and in situ data. *Remote Sens* 13:2431. <https://doi.org/10.3390/rs13132431>
- Nakada S, Isoda Y, Kusahara K (2003) Response of the coastal branch flow to alongshore variation in shelf topography off Toyama Bay. *Oceanogr Japan* 11(2):243–258 (in Japanese with English abstract)
- Nishida Y, Kanomata I, Tanaka I, Sato S, Takahashi S, Matsubara H (2003) Seasonal and Interannual Variations of the Volume transport through the Tsugaru Strait. *Oceanogr Jpn* 12(5):487–499. [https://doi.org/10.5928/kaiyou.12.487\(inJapaneseewithEnglishabstract\)](https://doi.org/10.5928/kaiyou.12.487(inJapaneseewithEnglishabstract))
- Ohshima K (1994) The flow system in the Japan Sea caused by a sea level difference through shallow straits. *J Geophys Res* 99(C5):9925–9940. <https://doi.org/10.1029/94JC00170>
- Onishi M, Ohtani K (1997) Volume transport of the Tsushima Warm Current, west of Tsugaru Strait bifurcation area. *J Oceanogr* 53(1):27–34
- Pedlosky J (1964) The stability of currents in the atmosphere and the ocean: Part I. *J Atmos Sci* 21:201–219. [https://doi.org/10.1175/1520-0469\(1964\)021<0201:TSOCIT.2.0.CO;2](https://doi.org/10.1175/1520-0469(1964)021<0201:TSOCIT.2.0.CO;2)
- Pedlosky J (1987) Geophysical fluid dynamics, 2nd edn. Springer-Verlag, New York
- Pond S, Pickard G (1986) Introductory dynamical oceanography, 2nd edn. Elsevier, New York
- Rosa AL, Isoda Y, Uehara K, Aiki T (2007) Seasonal variations of water system distribution and flow patterns in the Southern Sea Area of Hokkaido, Japan. *J Oceanogr* 63:573–588. <https://doi.org/10.1007/s10872-007-0051-4>
- Saitoh Y, Kuma K, Isoda Y, Kuroda H, Matsuura H, Wagawa T, Takata H, Kobayashi N, Nagano S, Nakatsuka T (2008) Processes influencing iron distribution in the coastal waters of the Tsugaru Strait, Japan. *J Oceanogr* 64:815–830. <https://doi.org/10.1007/s10872-008-0068-3>
- Sasaki Y, Minobe S, Miura Y (2014) Decadal sea-level variability along the coast of Japan in response to ocean circulation changes. *J Geophys Res* 119:266–275. <https://doi.org/10.1002/2013JC009327>
- Schaeffer A, Gramouille A, Roughan M, Mantovanelli A (2017) Characterizing frontal eddies along the East Australian Current from HF radar observations. *J Geophys Res* 122:3964–3980. <https://doi.org/10.1002/2016JC012171>
- Tanaka T, Hasegawa D, Okunishi T, Kaneko H, Ono T (2021) Internal hydraulic jump in the Tsugaru Strait. *J Oceanogr*. <https://doi.org/10.1007/s10872-020-00588-w>
- Tanno T, Kuroda H, Isoda Y, Aiki T (2005) Flow variations off Cape of Esan, northeast of Tsugaru Strait. *Bull Fish Sci Hokkaido Univ* 56:33–41 (in Japanese with English abstract)
- Thomas LN, Taylor JR, Ferrari R, Joyce TM (2013) Symmetric instability in the Gulf Stream. *Deep Sea Res* 91:96–110. <https://doi.org/10.1016/j.dsr.2.2013.02.025>
- Vallis GK (2006) Atmospheric and oceanic fluid dynamics: fundamental and large-scale circulation, 1st edn. Cambridge University Press, p 745
- Wada R, Waseda T, Nanjo H (2012) Nonlinear interaction of the Tsugaru Warm Current and tide in the Tsugaru Strait. *Ocean Dyn* 62:923–941. <https://doi.org/10.1007/s10236-012-0535-7>
- Wagawa T, Kawaguchi Y, Igeta Y, Honda N, Okunishi T, Yabe I (2020) Observations of oceanic fronts and water-mass properties in the central Japan Sea: repeated surveys from a glider. *J Mar Sys*. <https://doi.org/10.1016/j.jmarsys.2019.103242>
- Wakita M, Sasaki K, Nagano A, Abe H, Tanaka T, Nagano K, Sugie K, Kaneko H, Kimoto K, Okunishi T, Takada M, Yoshino J, Watanabe S (2021) Rapid reduction of pH and CaCO₃ saturation state in the Tsugaru Strait by the

- intensified Tsugaru Warm Current during 2012–2019. *Geophys Res Lett*. <https://doi.org/10.1029/2020GL091332>
- Yabe I, Kawaguchi Y, Wagawa T, Fujio S (2021) Anatomical study of Tsushima Warm current system: determination of principal pathways and its variation. *Prog Oceanogr*. <https://doi.org/10.1016/j.pocean.2021.102590>
- Yanagi T, Shimizu T, Lie HJ (1998) Detailed structure of the Kuroshio frontal eddy along the shelf edge of the East China Sea. *Cont Shelf Res* 18:1039–1056. [https://doi.org/10.1016/S0278-4343\(98\)80005-8](https://doi.org/10.1016/S0278-4343(98)80005-8)
- Yasuda I, Okuda K, Hirai M, Ogawa Y, Kudoh H, Fukushima S, Mizuno K (1988) Short-term variations of the Tsugaru Warm current in autumn. *Bull Tohoku Reg Fish Res Lab* 50:153–191 ((in Japanese with English abstract))
- Yasui T, Abe H, Hirawake T, Sasaki K, Wakita M (2022) Seasonal pathways of the Tsugaru Warm Current revealed by high-frequency ocean radars. *J Oceanogr* 78:103–119. <https://doi.org/10.1007/s10872-022-00631-y>
- Yoshikawa Y, Masuda A, Marubayashi K, Ishibashi M, Okuno A (2006) On the accuracy of HF radar measurement in the Tsushima Strait. *J Geophys Res* 111:C04009. <https://doi.org/10.1029/2005JC003232>
- Yoshikawa Y, Masuda A, Marubayashi K, Ishibashi M (2010) Seasonal variations of the surface currents in the Tsushima Strait. *J Oceanogr* 66:223–232. <https://doi.org/10.1007/s10872-010-0020-1>
- Yoshikawa Y, Lee CM, Thomas LN (2012) the subpolar front of the Japan/East Sea. Part III: competing roles of frontal dynamics and atmospheric forcing in driving ageostrophic vertical circulation and subduction. *J Phys Oceanogr* 42:991–1011. <https://doi.org/10.1175/JPO-D-11-0154.1>

Publisher's Note

Springer Nature remains neutral with regard to jurisdictional claims in published maps and institutional affiliations.

Submit your manuscript to a SpringerOpen[®] journal and benefit from:

- Convenient online submission
- Rigorous peer review
- Open access: articles freely available online
- High visibility within the field
- Retaining the copyright to your article

Submit your next manuscript at ► [springeropen.com](https://www.springeropen.com)
